HYDRAULIC AND GEOMORPHIC CONTROLS ON THE EVOLUTION OF CLUSTER BEDFORMS IN GRAVEL-BED STREAMS

by
Thanos Papanicolaou[1]
Lisa L. Ely[2]

[1]Department of Civil and Environmental Engineering
The University of Iowa
Iowa City, Iowa 52242-1527

[2] Department of Geological Sciences
Central Washington University
Ellensburg, Washington 98926

State of Washington Water Research Report WRR-21
U.S. Geological Survey Grant No. 02HQGR0139

For the period August 1, 2002 to July 31, 2005

Technical Report No. 452

IIHR—Hydroscience & Engineering
College of Engineering
The University of Iowa
Iowa City IA 52242-1585

August 2005

ACKNOWLEDGEMENTS

The activities on which this publication is based were supported in part by the Department of the Interior, U.S. Geological Survey, through the State of Washington Water Research Center, Grant Agreement No. 02HQGR0139. The views and conclusions contained in this document are those of the authors and should not be interpreted as necessarily representing the official policies, either expressed or implied, of the U.S. Government.

TABLE OF CONTENTS

LIST OF TABLES

LIST OF FIGURES

I. INTRODUCTION

The overall objectives of this collaborative study were to investigate the specific hydraulic conditions that control the evolution of cluster bedforms in both laboratory and field settings, and investigate the corresponding effects of the clusters on near-bed turbulence and channel stability. A cluster microform is a grouping of sediment particles, usually around a larger anchor sediment particle, against which a stoss of imbricate clasts develops and behind which a wake tail grows (Brayshaw, 1984; Billi, 1988; Church et al., 1998; Strom et al., 2004b). Cluster bedforms may play a role in the rate of gravel transport through a stream (Billi, 1988; Brayshaw et al., 1983; Brayshaw, 1984; De Jong, 1991; Naden and Brayshaw, 1987; Church et al., 1998; Strom et al., 2004b), and have been shown to provide important habitat for fish and stream invertebrates (Biggs et al., 1997; Boelman and Stein, 1997). Understanding the hydraulic conditions under which these bedforms develop and disintegrate is critical for managing, restoring and maintaining aquatic stream habitats in disturbed, natural and flow-regulated streams.

Particle clusters are a morphologic bed feature in gravel bed rivers termed “cluster microforms.” We here refer to cluster microforms as any organized three dimensional (3D) grouping of particles in the surface layer of a gravel bed stream (Papanicolaou et al., 2003). Included in this grouping are the classic “pebble cluster” of Dal Cin (1968) and Brayshaw (1984), and other observed shapes such as comet, ring, heap, and line type clusters (de Jong, 1995; Kozlowski and Ergenzinger, 1999; Strom et al., 2005a). The development and presences of these bed features is believed to be exemplary of a three fold feedback process between the flow field, bedload motion, and developed bedforms (such as cluster microforms).

Clusters are believed to form during the recession of a high flow event capable of transporting and depositing particles large enough to form an anchor clast that begins to impede smaller particles during waning stages of the flow event and/or during subsequent flow events (Dal Cin, 1968; Brayshaw, 1984; De Jong, 1991; Reid et al., 1992; Church et al., 1998). Clusters are typically formed as individual discrete structures, often protruding above the gravel bed surface (Brayshaw, 1984; Reid et al., 1992); however, other studies have shown that clusters form as interconnected structures in a reticulate pattern (Church et al., 1998; Hassan and Church, 2000).

II. LABORATORY AND NUMERICAL COMPONENT

A. Laboratory and Numerical Objectives

The first of two objectives for this study is to carry out an investigation of flow around a self-occurring cluster through a complementary laboratory experiment and 3D numerical simulation of the same cluster topography and flow conditions. The benefit of conducting a joint experimental and numerical investigation of flow around a self-occurring cluster is that experimental point measurements of velocity can be used to validate a 3D numerical model. Once that is accomplished, the 3D simulation can be used to investigate, in much greater detail, the spatial variation of the main flow variables, viz. mean velocity, turbulence statistics, pressure, and bed shear stress. Concurrent with this objective is to demonstrate the use of numerical modeling for predicting rough wall flows in hydraulic and geophysical applications. Typically, computational fluid dynamics (CFD) schemes and codes have spawned from mechanical and aerospace engineering applications and have been applied, in some cases, to geophysical applications without careful examination of basic underlying principles and assumptions of the methods. The second objective is therefore to point out some limitations and recommendations for CFD modeling of hydraulic and geophysical flows, where the presence of rough boundaries is a controlling element of the flow.

B. Experimental Arrangement

The experiments were conducted in a 21.2 m long, 0.9 m wide, tilting water-recirculating flume. The headbox of the flume is equipped with a honeycomb structure to provide rectilinear flow. Flow rate is regulated by use of a combination of one fixed speed pump and one variable speed pump, and was measured via a Venturi and water/mercury U-tube manometer. Tail water is controlled by the use of different combinations of rods placed spanwise at the free-fall exit of the flume. Rulers pre-placed along the length of the wall are used to determine flow uniformity; uniformity across the test section is also ensured by comparing velocity profiles at the upstream and downstream points in the test section.

The test section where clusters were developed and velocity measurement taken is 3.8 m in length, and is located 16.8 m downstream of the headbox to ensure fully developed flow. The test section is made of 4 layers of tightly packed glass spheres, diameter d=8 mm — creating a porous, uniform rough bed on which clusters form. Atop this uniform roughness layer, movable glass spheres (d=8 mm) are placed as the source sediment for cluster development (Fig. 1) (Strom et al., 2004). The ratio of flume width to flow depth, b/h, was kept > 5 to negate effects of narrow channel wall driven secondary currents (Nezu and Nakagawa, 1993). Wall effects are determined to be minimal at a distance of 10 cm from the flume walls (Vanoni and Brooks, 1957); all experiments are conducted at a distance greater than this from the side walls. Furthermore, the ratio of the average flow depth, h, to the cluster height, h_c, is such that $h/h_c > 4$ to ensure that cluster effects are not felt at the free surface (Shamloo et al., 2001).

C. <u>Procedures</u>

Clusters were naturally formed from a non-clustered bed of spherical glass particles, diameter d=8 mm, following the methodological procedures of Strom, Papanicolaou, Evangelopoulos, and Odeh for Test Series A. Specifically, the test particles were placed in the test section atop the uniform roughness bed at a particle-to-particle spacing of 6d. This spacing ensured an isolated roughness regime (i.e. a non-clustered bed) for the initial conditions of the test. For an isolated roughness regime the wake of an upstream particle does not interfere with a subsequent downstream particle (Morris, 1955). Once the initial condition was set, water was gently introduced to the flume and raised to the preset stress condition.

This was done for the cluster forming condition of $1.5\tau_{cr}^{*}$ (Strom et al., 2004, , test Series A) since it was found that clusters form from a non-clustered state at the sediment and hydraulic conditions specified for this test case. Here τ_{cr}^{*} represents the incipient motion condition for the entrainment of an isolated particle, $\tau_{cr}^{*} = u_{*cr}^{2}/(SG-1)dg$, $u_{*} = \sqrt{\tau/\rho}$ is the friction velocity, t is the bed shear stress, r is fluid density, SG is the specific gravity of the entrainable sediment, and g is the acceleration of gravity. τ_{cr}^{*} is

based on a 2% probability of entrainment criterion for the initial bed setup, meaning that 2 out of 100 available grains will move over a bursting period (Papanicolaou et al., 2002). For this test configuration, clusters start to breakup at $2.25\tau_{cr}^{*}$ (Strom et al., 2004). Table 1 summarizes the hydraulic conditions for cluster formation and the subsequent velocity measurements.

The experiments were run until a clustered bed formed and reached an equilibrium state where overall cluster geometry, cluster spacing, and average bedload transport rate did not change as a function of time. At these equilibrium conditions, for $1.5\tau_{cr}^{*}$, clusters have an average longitudinal spacing, λ_x, to cluster height of $\lambda_x / h_c = 15$ (Strom et al., 2004).

At this point, the original spherical glass particles (*SG*=2.58) used to form the clusters were carefully replaced with equal diameter lead particles (*SG*=11.3). This was done to ensure that no particles in the clusters would alter the flow field during the velocity measurements by becoming entrained. A similar methodology was followed by Papanicolaou et al. (2001) to measure the mean flow characteristics over varying packing densities of spheres.

Velocity measurements were carried out using 2D laser Doppler velocimetry (LDV). LDV was chosen for the small measuring volume of the laser, vertical diameter of 100 mm and length of 1.3 mm, which allowed for multiple measurement points to be made within the wake region of a cluster, cluster height $h_c = 6.5$ mm (Fig. 1). The LDV system consisted of a 5 W Coherent Innova 90 laser, TSI ColorBurst separator, TSI ColorLink multicolor photomultiplier and a Macrodyne FDP module. The 2D LDV system was set up to measure longitudinal and vertical velocities in coincidence mode. A 100 kHz positive shift was added to both color channels to allow for proper detection of bidirectional fluid motion. 750 measurements per location in the vertical were made at an average data acquisition rate of 5-10 Hz by seeding the flow with 10 mm diameter, neutrally buoyant particles. There was no statistical difference in the mean between samples containing 750 measurements and those containing 5000 at 95% confidence (p-value = 0.072). The data sample rate of 5-10 Hz was sufficient to captures the large scale motion, which has an average bursting period $T_B = 3U_{\max} / h = 0.4$ sec or 2.5 Hz. However, the sample rate of 5-10 Hz is unable to capture the full spectrum of scales

down to the dissipative length $\eta \approx h/\mathrm{Re}_*^{3/4} = 0.2$ mm, where $\mathrm{Re}_* = u_* h/\nu$. In order to do this, a sample frequency of 100 Hz or greater would be recommended to resolve the full range of scales, based on the dimensionless wavenumber $L_x k_{\max} > 100$ where L_x is the macro length scale, and $k_{\max}$ is the maximum wavenumber beyond which is noise (Nezu and Nakagawa, 1993).

Beam velocities were collected at a 45° angle to the x, y coordinate system (Fig. 1), combined, and rotated to physical velocities *U* and *V* through a coordinate transformation. The biasing correction scheme of McLaughlin and Tiederman (1973) was employed to account for biasing towards higher velocity. The result of this were time series of longitudinal and vertical velocity *U=U(x,y,t)* and *V=V(x,y,t).* These series were then ensemble averaged to produce *u(x,y), v(x,y),* and second order moments, $\overline{u'u'} = \overline{u'u'}(x,y)$, $\overline{v'v'} = \overline{v'v'}(x,y)$, and $\overline{u'v'} = \overline{u'v'}(x,y)$.

Forty velocity profiles were taken over a longitudinal line of clusters in the developed cluster bed. These profiles showed that clusters represent, on an average, isolated roughness elements at a spacing of $\lambda_x / h_c = 15$. For this reason a single representative cluster was chosen for a more detailed examination (Fig. 2). It was ensured from the 40 velocity profiles that wake effects of the cluster chosen for the analysis did not extend to the downstream cluster, nor were there effects from upstream clusters. In addition, mean velocity and turbulent statistics due to wake effects from an obstacle are reported to be fully recovered at a downstream distance of $x/h_c = 10-20$, where *x* is the longitudinal downstream distance (Paola et al., 1986; Buffin-Bélanger and Roy, 1998; Shamloo et al., 2001).

Five additional, more detailed velocity profiles were then obtained in the five major flow regions surrounding the cluster. These profiles pertain to, region 1: the unaffected approach velocity, *x=0* mm; region 2: the decelerated stoss region, *x=28* mm; region 3: the accelerated region atop the cluster, *x=54* mm; region 4: the cluster wake, *x=123* mm; and region 5 the far downstream region where flow has returned to an unaffected state, *x=238* mm (Fig. 3). The velocity profile at *x=0* mm was compared to a velocity profile at the same location made without any clusters in the test section. The comparison revealed no difference in the two profiles, showing that the velocity profile at *x=0* mm represents a flow undisturbed by the cluster.

D. Experimental Results

Part of the purpose for the experimental data is to obtain accurate flow quantity measurements for this particular morphologic arrangement to be used as validation for the 3D numerical model. The 3D model will then in turn offer more detailed information of the flow surrounding the cluster than could be obtained experimentally due to physical constraints of the cluster geometry and LDV method. LDV measurements cannot be collected below 1 mm from to top of the particles within the bed (Fig. 1). Additionally, measurements along the flanks of the cluster close to the bed are not possible because scattered light from the physical presence of the cluster overpowers the photodetector, making velocity readings indistinguishable from reflected noise. Since the data is to be used for comparison purposes with the numerical simulation, we wish to validate the experimental data by comparing it to well established trends for similar conditions.

The velocity profiles for the 5 locations are depicted in Fig. 4. Fig. 4(a) shows that the cluster has an effect on the wall region of the flow, $y/h \le 0.2$, while this effect is minimized in the outer region, $y/h \ge 0.2$. The only exception to this is right over the top of the cluster, *x=54* mm, where there is a slight acceleration of the flow up to $y/h = 0.46$, at which point no variation in the profiles can be detected. This is consistent with the findings of Shamloo et al. (2001) for flow regimes with $h/h_o > 4$, where h_o is the height of a hemisphere protruding from a flume bed. For our case $h/h_c = 11.8$.

Within the region $y/h \le 0.2$, the effects of the cluster are reflected in the velocity profiles. As expected, at the leading tip of the cluster (*x*=28 mm), i.e. the cluster stoss, the flow is significantly retarded (Fig. 4). Moving up away from the bed the velocity increases and then decreases to a minimum at a height of *y*=2.5 mm, corresponding to the apex of the leading sphere in the cluster. From this point the velocity rapidly increases as the top of the cluster is reached. Atop the cluster, *x*=54 mm, the flow is accelerated compared to the undisturbed state with a stiff gradient near the cluster and a slight positive shift in the velocity profile in the outer flow (Fig. 4). In the wall region of the wake, $y/h \le 0.2$, *x*=123 mm, the velocity is again retarded compared to the unaffected state. Although flow is retarded, no recirculation is evident from this profile as $\partial u/\partial y$

remains greater than 0 throughout the depth. By x=238 mm, $x/h_c = 18$, the mean velocity profile shows a return to the undisturbed state (Fig. 4).

Qualitatively, the measured velocity distributions behave as expected for flow over obstacles. For conditions upstream of the cluster, region 1 at x=0 mm, the flow is expected to be 2D, steady, uniform, and in equilibrium, i.e. turbulence production is approximately equal to dissipation. If this is true, the distribution of the longitudinal averaged velocity, *u(y),* should adhere to the form of the log law valid for this particular experimental setup. For smooth wall flows the log law is written as,

$$u^+ = \frac{1}{k}\ln y^+ + B \tag{1}$$

where,

$$u^+ = \frac{u}{u_*},\ \ y^+ = \frac{yu_*}{\nu},\ \ k_s^+ = \frac{k_s u_*}{\nu} \tag{2}$$

the constant $\kappa = 0.4$, ν is the kinematic viscosity of the fluid, k_s is the roughness length scale, and B is the constant of integration equal to $B = 5.5$ for smooth wall flows, i.e. $k_s^+ < 4$. For walls with roughness B is a function of hydraulic roughness, $B = B(k_s^+)$ expressed as,

$$B(k_s^+) = \frac{1}{\kappa}\ln k_s^+ + B_r \tag{3}$$

where B_r is the constant of integration for rough wall flows. For the present experimental conditions, in which the bed is rough and porous, the dimensionless coordinate normal to the bed, y^+, is defined as,

$$y^+ = \frac{(y + y_o)u_*}{\nu} \tag{4}$$

where $y_o = 0.25k_s$ (Song and Chiew, 2001). This is done to account for the displacement of the zero velocity reference level from the top of the bed to some location within the porous bed (Fig. 1). Substituting Eq. 3 and 4 into Eq. 1 yields the form of the log law valid for the current experimental conditions,

$$u^+ = \frac{1}{\kappa}\ln\left(\frac{y + y_o}{k_s}\right) + B_r \tag{5}$$

where $B_r = 8.5$ for fully rough conditions ($k_s^+ > 70$) (Nezu and Nakagawa, 1993; Kironoto and Graf, 1994). In the present case, $k_s^+ = 274$, i.e. fully rough, with Reynolds number $\mathrm{Re} = hU_{bulk}/\nu = 31150$ where U_{bulk} is the mean bulk velocity of the flow.

Comparing the experimental data at x=0 mm to Eq. 5 reveals that the velocity profile is well described by the logarithmic function (Fig. 5(a)) u_* computed from a regression fit of the experimental data to the form of Eq. 5, fixing B_r, κ, and $k_s = 0.008$ m gives the values of $u_* = 0.039$ m/s (Fig. 5(a)). This is identical to a u_* computed from the uniform open channel flow equation $u_* = \sqrt{ghS} = 0.039$ m/s. Fig. 4(b) plots velocity profiles on a logarithmic scale in the 5 different regions of the cluster. Fig. 4(b) assesses the validity of a logarithmic description of the velocity distribution, Eq. 5, in each of these regions. From this plot we see that a log law type relation only holds for regions 1 (x=0 mm) and 5 (x=238 mm) over the entire flow depth; these are the two locations unaffected by the presence of the cluster. In the other 3 regions the logarithmic distribution breaks down in the near-wall region around the cluster. Therefore, it follows that the use of the wall functions approach to numerically describe flow around the cluster in this region will not be valid. This is because the wall functions approach assumes a logarithmic distribution to match between the wall ($y^+ = 0$) and the first grid point off the wall situated at $y^+ \sim 30 - 300$.

Distributions of turbulence quantities over a rough wall are not as well defined as turbulence quantities over smooth wall (Nezu and Nakagawa, 1993). In general, turbulence intensities will decrease from the wall to the free surface after the initial peak close to the bed where turbulence production is at a maximum; though varying roughness configuration can have significant effects on the distribution of turbulence statistics in the wall region (Raupach et al., 1991; Krogstad and Antonia, 1999). Fig. 5(b) shows the comparison between the experimental data in region 1 and the smooth wall semi-empirical intensity profiles of Nezu and Nakagawa (1993). The measured data behave in an expected manner; with the streamwise intensity $u_{rms}^+ = \sqrt{\overline{u'^2}}/u_*$, exceeding vertical intensity, v_{rms}^+, and the damping of u_{rms}^+ and v_{rms}^+ in the wall region ($y/h \le 0.3, y^+ \le 860$). This damping effect is likely due to the breakup of the near-wall structures by the presence of roughness. Reynolds stress, $-uv^+ = -\overline{u'v'}/u_*^2$, also decreases from the bed to

the free surface after the initial peak (Fig. 5(c)), and retains its linear distribution in the outer region.

E. Numerical Simulation

Numerical simulation of the average flow patterns around a cluster is carried out by solving the Reynolds averaged Navier-Stokes (RANS) equations. RANS formulations have been shown to be accurate in simulating average 3D flow quantities around protruding obstacles in boundary layers (Lien and Yee, 2004). The RANS formulation of the governing continuity and momentum equations for an incompressible fluid are,

$$\partial_i u_i = 0 \tag{6}$$

$$\partial_t u_i + u_j \partial_j u_i = -\frac{1}{\rho}\partial_i p + \nu \nabla^2 u_i - \partial_j \overline{u'_i u'_j} \tag{7}$$

where u is the time averaged velocity vector $u_i(x,y,z) = U_i(x,y,z,t) - u'_i(x,y,z,t)$, p is pressure, and i,j=1,2,3, ($u_1 = u$, $u_2 = v$, and $u_3 = w$). Closure to Eqs. 6 & 7 is obtained through a model for the turbulent stress tensor $\overline{u'_i u'_j}$.

The selection of a turbulence closure model is based on the following two criteria: (1) that the model is able to handle the three roughness regimes, i.e. hydrodynamically smooth, transitional, and fully rough surfaces; and (2) that the model is able to describe separated flows (Patel, 1998). This is an important and necessary capability for turbulence models to have when used to calculate flows in geophysical applications since boundaries are often rough and contain protrusion that cause separation, e.g. large rocks, bedforms, and buildings. While various forms of the $k-\varepsilon$ model with wall functions are the most commonly used and documented models, a variant of the $k-\omega$ model is here chosen to model turbulence effects inside the wall region of the flow. The use of $k-\omega$ in this region is advantageous because of its ability to be integrated down to the wall without the use of damping functions, and its ability to intrinsically handle roughness by specifying the boundary condition for ω at the wall as a function of roughness height (Wilcox, 1993; Patel, 1998). Using a near-wall $k-\omega$ model therefore allows for the elimination of wall functions in accounting for roughness effects. This is a desirable attribute of a turbulence model for our application, and similar geophysical applications,

since the validity of wall functions break down in separated flows (Patel et al., 1991), such as flow over a cluster microform (Fig. 4(b)).

The general 3D finite volume commercial CFD solver FLUENT is employed to compute the velocity and pressure fields using a pressure-Poisson based method (SIMPLE) and two-equation turbulence closure. For all of the following simulations, the steady-state segregated solver in FLUENT is used with 2^{nd} order upwind discretization for the momentum equations, including the convective terms, and 1^{st} order upwind discretization for the convective terms in the k and ω equations. FLUENT is widely used and has been employed for other hydraulic engineering and geophysical applications (e.g., Hodskinson and Ferguson, 1998; Nicholas and Sambrook Smith, 1999; Karim and Ali, 2000; Nicholas, 2001). However, most of these applications have used the wall functions approach.

F. <u>Turbulence Model</u>

The turbulence model used in the present simulation of flow over a cluster microform, is the shear stress transport (SST) model of Menter. The SST model uses $k-\omega$ in the wall region and incorporates a blending function to switch to $k-\varepsilon$ in the outer wall region. Use of the $k-\varepsilon$ model in this region is recommended due to the relative insensitivity of $k-\varepsilon$ to levels of incoming flow turbulence when compared to the $k-\omega$ model. $k-\omega$ utilizes a transport equation for the turbulent kinetic energy, $k=\overline{u_i' u_i'}/2$, and specific turbulent dissipation, $\omega=\varepsilon/k$ where ε is the turbulent dissipation, to calculate the eddy viscosity, ν_T, and closes Eq. 6 and 7 using the Boussinesq hypothesis for turbulent flow,

$$\overline{u_i' u_j'}=\frac{2}{3}k\delta_{ij}-2\nu_T S_{ij} \tag{8}$$

where $S_{ij}=(\partial_j u_i+\partial_i u_j)/2$ is the mean rate of strain, and δ_{ij} is the Kronecker delta.

SST transport of the turbulent principal stress is accomplished through the concept that turbulent stress is proportional to turbulent kinetic energy (Menter, 1994) through the eddy viscosity formulation,

$$\nu_T = \frac{k}{\max\left(\frac{\omega}{\alpha^*}, \frac{\Omega F_2}{a_1}\right)} \tag{9}$$

where $\Omega = \sqrt{2\Omega_{ij}\Omega_{ij}}$ is the mean rate of rotation tensor, $a_1 = 0.31$ is the proportionality constant between the turbulent stress and *k*,

$$F_2 = \tanh(\Phi_2^2), \quad \Phi_2 = \max\left(2\frac{\sqrt{k}}{0.09\omega y}, \frac{500\nu}{\omega y^2}\right) \tag{10}$$

and,

$$\alpha^* = \alpha_\infty^*\left(\frac{\alpha_0^* + \mathrm{Re}_t/R_k}{1 + \mathrm{Re}_t/R_k}\right) \tag{11}$$

where $\mathrm{Re}_t = k/\omega\nu$, and the model constants are $\alpha_\infty^* = 1$, $\alpha_0^* = \beta_i/3$, $\beta_i = 0.072$, and $R_k = 6$.

As previously noted, the significant advantage of the SST model in relation to rough wall flows is that it can predict the effect of roughness through the boundary condition of ω at the wall, ω_w, rather than through the use of wall functions. The SST model in FLUENT (Wilcox, 1993; FLUENT Inc., 2003) defines ω_w,

$$\omega_w = \frac{\nu}{u_*^2\omega^+} \tag{12}$$

where,

$$\omega^+ = \min\left(\omega_w^+, \frac{6}{\beta_\infty^*(y^+)^2}\right) \tag{13}$$

$\beta_\infty^* = 0.09$, and,

$$\omega_w^+ = \begin{cases} \left(\frac{50}{k_s^+}\right)^2 & k_s^+ < 25 \\ \frac{100}{k_s^+} & k_s^+ \geq 25 \end{cases} \tag{14}$$

Therefore roughness effects can be obtained through ω_w by a declaration of the roughness length k_s (Eq. 12-14). Boundary conditions for the velocity and turbulent

kinetic energy at the wall are $u_i = 0$ and $\frac{\partial k}{\partial n} = 0$, where n is the direction normal to the wall (FLUENT Inc., 2003).

G. Roughness Simulation Using the Near-Wall SST Model

Wall roughness effectively downshifts the rough wall velocity profile relative to that of flow over a smooth wall. This is due to extraction of momentum caused by the roughness elements. The downshifting affect of roughness is expresses in the parameter ΔB in the log law (Eq. 1) as,

$$u^+ = \frac{1}{\kappa}\ln y^+ + B - \Delta B \tag{15}$$

where ΔB is a function of the hydraulic roughness, $\Delta B = \Delta B(k_s^+)$. Accurate prediction of this downshifting needs to be verified before moving to rough wall flows with the presence of a cluster.

The ability of the near-wall SST model implemented in FLUENT to effectively handle boundary roughness was tested in a 2D domain without the presence of a cluster (Strom et al., 2005b). This was done by computing the functional response of $\Delta B = \Delta B(k_s^+)$ over a range of roughness, $4 \le k_s^+ \le 1750$, $0.0026 \le k_s/h \le 0.4000$, and comparing the computed results to ΔB predicted by the log law in the fully rough regime,

$$\Delta B = B - 8.5 + \frac{1}{\kappa}\ln k_s^+ \tag{16}$$

and the empirical relation of Cebeci and Bradshaw (1977) in the transitional regime,

$$\Delta B = \left(B - 8.5 + \frac{1}{\kappa}\ln k_s^+ \right) \sin[0.4258(\ln k_s^+ - 0.811)] \tag{17}$$

For each value of k_s, ΔB was computed by a regression fit of the form of Eq. 15 to the fully developed velocity profile with B = 5.5. Table 2 and Fig. 6 summarize the conditions and results of the comparison between ΔB calculated from the computational results and ΔB predicted by Eqs. 16 and 17. The variable f in Table 2 is the friction factor computed from the model and defined as $f = 8\tau/\rho U_{bulk}$. Results of the simulation show that the near-wall SST model implemented in FLUENT is capable of predicting rough

wall effects over a large range of roughness heights spanning both the transition and fully rough regimes ($4 \le k_s^+ \le 1750$ and $0.0026 \le k_s/h \le 0.4000$).

H. Mesh

The 3D cluster mesh was produced using information obtained from analysis of the digitally imaged experimental cluster bed. (*x*,*z*) coordinates pertaining to the center of each particle in the cluster were extracted from the image (Fig. 2 & 3). The grid was then generated accounting for the geometry of the particles, 8 mm diameter spheres, and the cluster height, $h_c = 6.5$ mm. Particles in the cluster that were tightly packed in a similar fashion as the uniform roughness bed were treated as a solid polygonal object with imposed roughness equal to that of the uniform roughness bed. Particles not touching were treated as individual obstacles jutting out of the bed. This results in an obstacle that occupies the same footprint as the experimentally developed cluster with the same corresponding height, $h_c = 6.5$ mm (Fig. 7 & 8).

For the numerical simulation, the experimental domain and conditions shown in Fig. 3 and Table 1 were nondimensionalize such that $h = 1$, $U_{bulk} = 1$, $q = 1$, $\rho = 1$, $\nu = 1/\mathrm{Re}$, $k_s^+ = 274$, $\mathrm{Re} = 31150$, and $u_*/U_{bulk} = 0.085$. The resulting computational domain is $1h \times 1.3h \times 3.25h$ (height $\times$ width $\times$ length). Nondimensionalization allows easier comparison with other results and allows for simulations with different hydraulic conditions to be made with the same mesh by varying Re and k_s.

An un-structured meshing technique, call paving, was used to generate a mesh containing only quadrilateral elements in the cluster region. This region was then connected with the rest of the domain in which less densely spaced structured meshing was used (Fig. 7). Grid spacing in the (x,z) direction ranged between $6 \le y^+ \le 17$ (0.0023*h*-0.0065*h*) in the cluster region to $y^+ = 70$ (0.026*h*) outside the cluster region. The resulting grid spacing is adequately refined for a detailed RANS study at Re=31150 (e.g. Sofialidis and Prinos, 1999; Lien and Yee, 2004).

Modeling the cluster as a polygonal object allowed for the location of the first grid point normal to the wall to be set at $y^+ = 0.1$ throughout the domain. This was accomplished by keeping successive computational planes in the vertical direction

parallel with the wall (Fig. 9). Moreover, this eliminates the excessive grid points in the horizontal directions that would be required if square or spherical boundary shapes would have been used in defining the cluster. This spacing, with the first grid point at $y^+ = 0.1$, was set to satisfy the grid refinement normal to the wall required for SST in order to handle the increased gradients near the wall caused by roughness (Patel, 1998). 56 nodes were used in the vertical direction throughout the domain (Fig. 9), and the grid stretching factor was set to 1.2 at the wall. This results in a minimum grid spacing in the vertical of $y^+ = 0.1$ at the wall and a maximum grid spacing of $y^+ = 272$ at the free surface. Grid independence is obtained at this vertical spacing, 56 nodes with the first grid point located at $y^+ = 0.1$. In total, the resulting mesh is composed of 1.7×10^6 computational elements.

I. <u>Boundary Conditions</u>

The following boundary conditions are used to obtain a 3D steady-state solution for the mean velocity and turbulence quantities. The sides and top of the domain are modeled as planes of symmetry. This results in the free surface being modeled as a moving plane wall. This is taken to be a reasonable approximation for the present cluster geometry and flow conditions since free surface effects due to the cluster are negligible for a flow depth to cluster height ratio of $h/h_c = 11.8$ (Shamloo et al., 2001). This approximation would not be valid for flows over obstacles, or clusters, where $h/h_c \leq 4$. The outlet of the domain is treated as a mass outflow plane.

A 2D rough wall, fully developed solution of an unobstructed flow with periodic inflow and outflow boundaries was used to define inlet boundary conditions for the mean velocity profile, *u(y)*, turbulent kinetic energy profile, *k(y)*, and the turbulent specific dissipation profile, $\omega(y)$. A profile from the 2D solution was used as the inlet conditions instead of the experimental profile so that *u(y)*, *k(y)*, and $\omega(y)$ could be specified over the entire flow depth without the flow developing over the domain. The 2D solution was obtained by varying k_s until ΔB from the model matched ΔB from the experimental LDV data profile at x=0 mm. The results from the 2D simulation well matched the experimental conditions without adjustment of model constants; ΔB and k_s^+ values were

equal to $\Delta B = 10.99$ and $k_s^+ = 274$ for the experiment, and $\Delta B = 11.02$ and $k_s^+ = 258$ for the simulation.

J. Model Validation-Results

We now examine the capabilities and performance of the model in predicting the mean longitudinal velocity *u*, turbulent kinetic energy *k*, and eddy viscosity ν_T of the flow over the cluster. Calculated model output normalized by U_{bulk}, *h*, and ν are compared to the experimental data in the 5 flow regions over the cluster. Fig. 10 depicts a profile view of the calculated velocity profiles over the cluster section in each of these regions.

The near-wall SST model adequately predicts the mean longitudinal velocity profiles at each of the 5 locations along the cluster (Fig. 11). The undisturbed profile at x=0 mm (region 1) is plotted in each figure to give a better idea of the effect the presence of the cluster has on the mean streamwise flow compared to a case without the presence of the cluster. Similar to the experiments, little disturbance due to the cluster is felt in the outer region of the flow ($y > 0.2h$), with the most pronounced effects in the outer region occurring atop the cluster at x=54 mm (Fig. 11(c)) Of note is the comparison of the computed profiles at x=0 mm and x=238 mm (Fig. 11(e)) This figure shows that the effects of the cluster are still being slightly felt at x=238 mm in the simulation. The model also performs well in the non-logarithmic zones of region 2 (x=28 mm) and region 4 (x=123 mm). This is a testament to the ability of near-wall modeling to capture the effects of rapidly accelerating and decelerating flows with separation and a rough boundary.

A note concerning the behavior of turbulent kinetic energy at the wall should be made. FLUENT uses a zero gradient boundary condition for turbulent kinetic energy, $\frac{\partial k}{\partial n} = 0$, at the wall, i.e. at $y=0$ (FLUENT Inc., 2003). If the wall is smooth, FLUENT predicts the expected result of k at the wall equal to zero, $k(x,0,z)=0$. If however the wall is rough, $y=0$ becomes the plane located somewhere within the roughness elements at which the mean velocity is equal to zero, i.e. the zero velocity plane. At this location the

mean velocity *u(x,0,z)* is zero but the fluctuating velocity *u'(x,0,z,t)* can be nonzero. Thus, *k(x,0,z)* is not equal to zero in the present simulation.

The near-wall SST model best predicts *k* in region 3 (*x*=54 mm) and region 4 (*x*=123 mm) due to the physical presence of the cluster (Fig. 12). In region 3, strong acceleration atop the cluster causes steep gradients near the wall and high turbulence production. In region 4, the shear layer in the wake of the cluster, at a height comparable to the height of the cluster, is responsible for the peak in *k*. This is observed in both the experimental and numerical simulations.

Although region 2 (the cluster stoss) is also strongly effected by the cluster presence, topographical differences in the actual physical cluster geometry and the mesh account for the differences between the model and experiment. The physical geometry of the leading particle in the cluster is defined by a sphere and hence has an apex protruding upstream around a height of approximately 1/2 the diameter of the sphere (Fig. 1). The mesh on the other hand is defined by a monotonically increasing line from the bed to the top of the cluster (Fig. 10). Flow at *x*=28 mm in the physical geometry diverge at the sphere apex away from (+*y* direction) and towards (-*y* direction) the bed, reaching a minimum at the sphere apex. In the computational domain, flow is predominately in the +*y* direction over the entire flow depth at *x*=28 mm, causing greater velocity at the same height as the apex in the physical domain. It is this topography difference between the physical and computation domains that the discrepancy in *k* at *x*=28 mm is ascribed to. This highlights the importance of using computational meshes that are representative of the physical conditions. While there are some discrepancies in the present study between the mesh and the physical conditions at *x*=28 mm, these discrepancies are very localized and do not greatly affect the rest of the solution.

Eddy viscosity for the experimental profiles was calculated as $\nu_T = -\overline{u'v'}/\partial u/\partial y$. Fig. 13 compares the calculated and experimental results. In general the model reasonably predicts ν_T when compared with the experimental data. One should point out that there is significant spread in the experimental data due to the scatter in $\overline{u'v'}$ and the sensitivity of ν_T to the calculation $\partial u/\partial y$. Computed ν_T correlates with the experiments most poorly at the cluster nose, *x*=28 mm. This is attributed to the previously mentioned

localized differences in topology between the leading particle in the physical cluster and the leading tip of the computational mesh.

Table 1: Conditions for cluster formation. Where S is slope, h is the flow depth, q is the volumetric discharge, Fr is the Froude number defined as $Fr = U_{bulk}/\sqrt{gh}$, and *b* is flume width.

	τ^*	S %	h (m)	q (m^3/s)	U_{bulk} (m/s)	Re	Fr	u_* (m/s)	b/h
$1.5\tau^*_{cr}$	0.012	0.2	0.077	0.036	0.46	31150	0.53	0.039	11.6

Table 2: Response of ΔB and f to changes in k_s^+ using the SST near-wall model in FLUENT with ω_o set by k_s at the wall. $^{\dagger}\Delta B$ calculated using Eqs. 16 and 17.

k_s^+	k_s/h	u_*	Calculated f	ΔB SST	$\Delta B^{\dagger}$	% Difference
4	0.0026	0.05	0.020	1.54	0.14	166.57%
9	0.0053	0.053	0.022	2.6	1.34	63.67%
19	0.010	0.059	0.028	4.92	3.38	37.22%
37	0.018	0.064	0.033	6.52	5.54	16.22%
57	0.026	0.068	0.037	7.55	6.90	9.03%
76	0.033	0.071	0.040	8.23	7.72	6.38%
123	0.050	0.076	0.046	9.3	8.93	4.03%
199	0.075	0.082	0.054	10.37	10.13	2.33%
283	0.100	0.087	0.061	11.24	11.01	2.07%
475	0.150	0.098	0.077	12.74	12.31	3.45%
695	0.200	0.107	0.092	13.81	13.26	4.07%
1191	0.300	0.122	0.119	15.26	14.61	4.38%
1750	0.400	0.135	0.146	16.25	15.57	4.28%

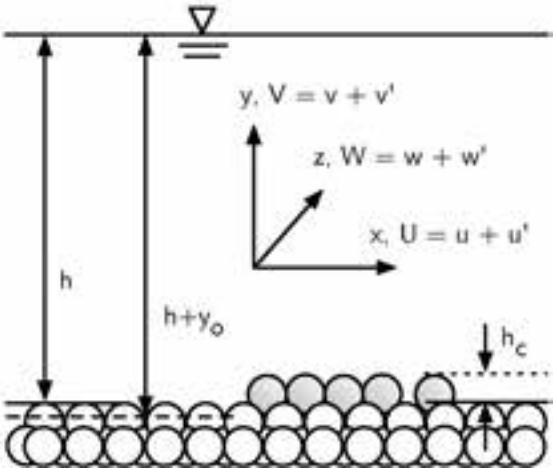

Figure 1: Coordinate system definition; vertical slice schematic. Grey particles represent a formed cluster atop the uniform roughness bed.

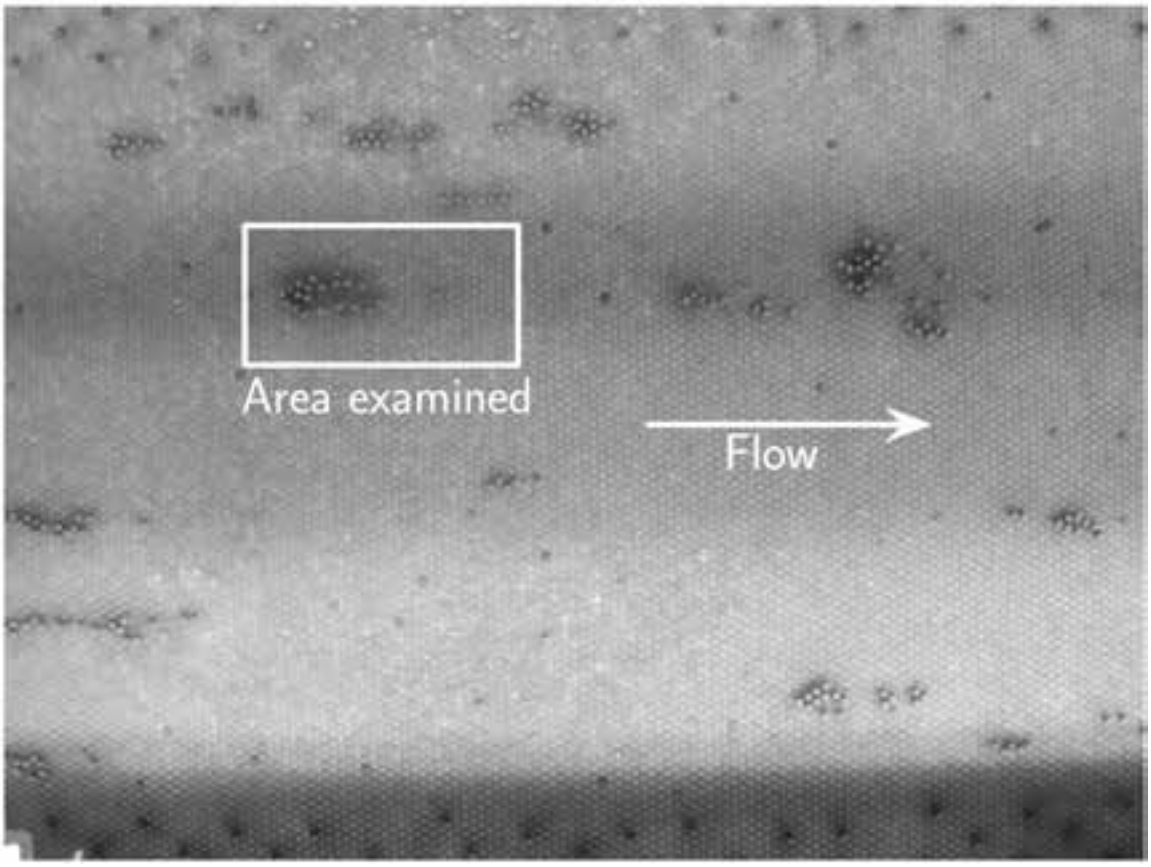

Figure 2: Plan view of self-occurring clusters. Light colored particles are the uniform roughness bed and the darker particles are the formed clusters and individual sediment particles.

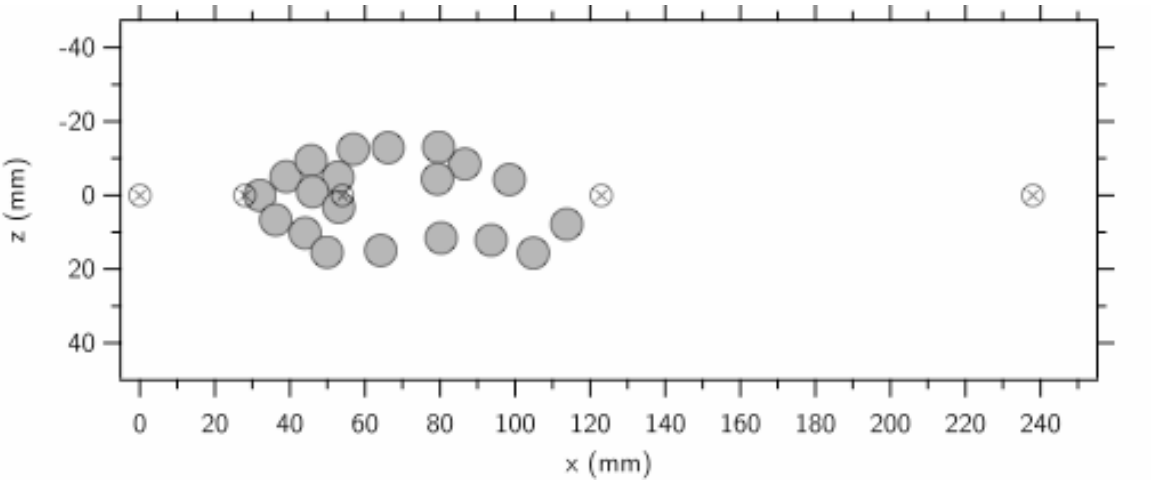

Figure 3: Plan view of the single cluster domain. Flow is from left to right, and points marked by ⊗ represent the velocity profile locations. x=0 mm = region 1, x=28 mm = region 2, x=54 mm = region 3, x=123 mm = region 4, and x=238 mm = region 5.

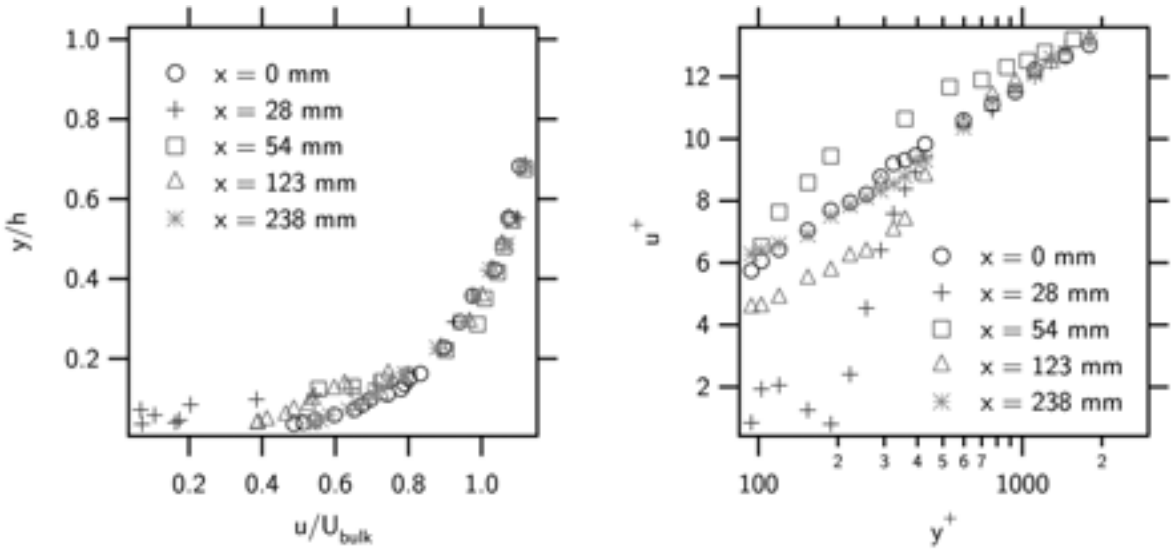

Figure 4: Experimentally measured velocity profiles at x=0 mm: approach velocity, x=23 mm: decelerated stoss region, x=54 mm: atop cluster, x=123 mm: wake, x=238 mm: return to unaffected state.

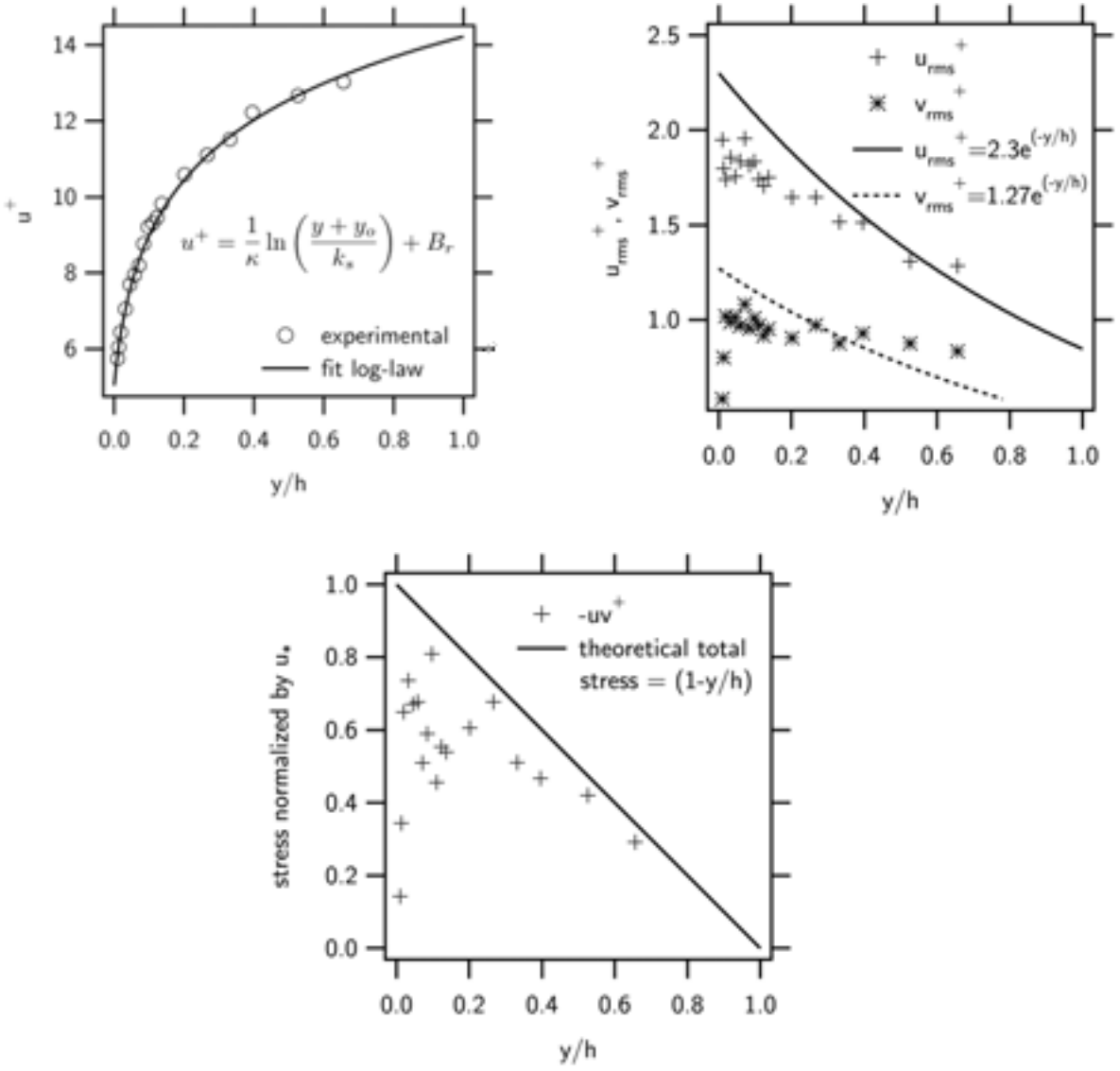

Figure 5: Experimental data. (a) streamwise velocity at x=0 mm compared with Eq. 5; (b) turbulent intensities at x=0 mm compared to Eq. 4.3 and 4.4 of Nezu and Nakagawa; and (c) Experimentally measured Reynolds stress $-uv^+$ at x=0 mm compared to the 2D uniform open channel theoretical total stress (turbulent + viscous stress) distribution.

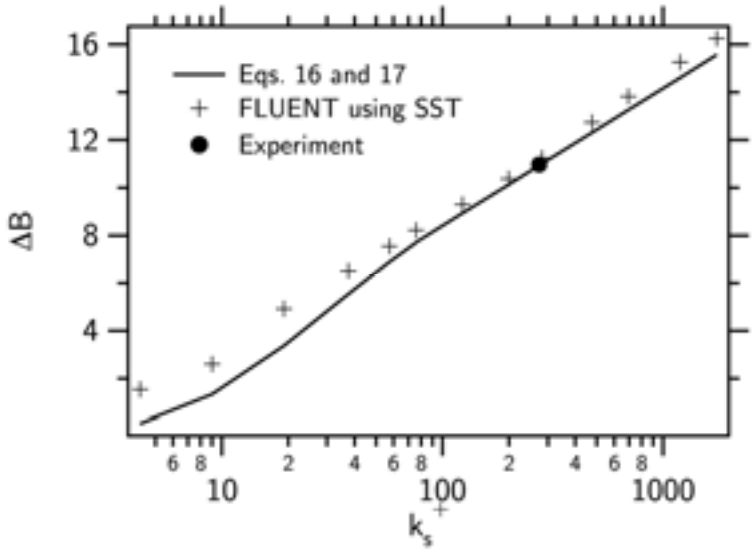

Figure 6: SST near-wall model predicted response of ΔB to changes in roughness, k_s^+, compared to Eqs. 16 and 17.

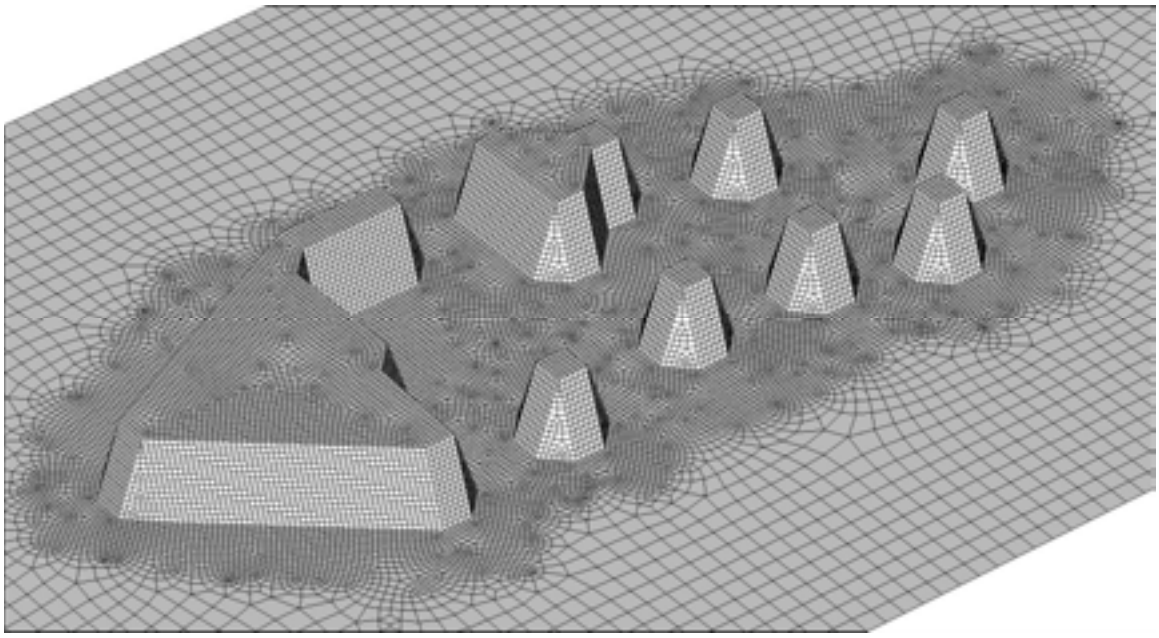

Figure 7: 3D view of cluster mesh geometry.

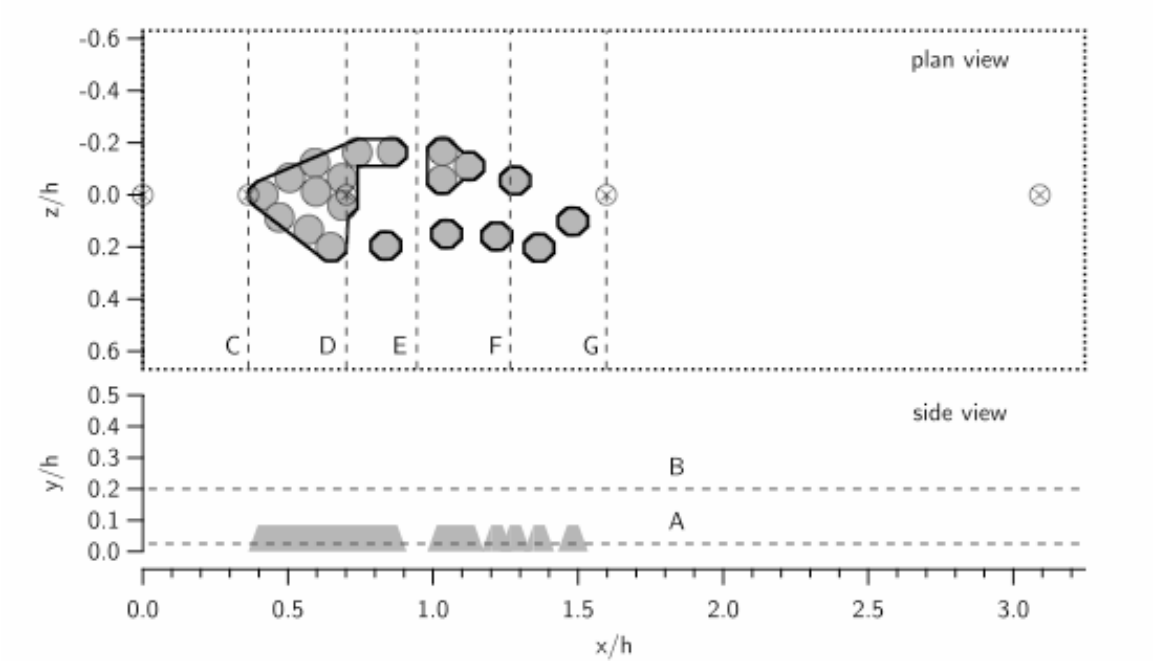

Figure 8: Footprint and side view of cluster mesh compared to the experimental cluster along with the location of key planes (A-G) examined in the solution. Grey spheres represent the experimentally formed cluster, the black overlaid line represents the footprint of the computational mesh, dotted lines are planes examined in the solution, and ⊗ marks the experimental velocity profile locations.

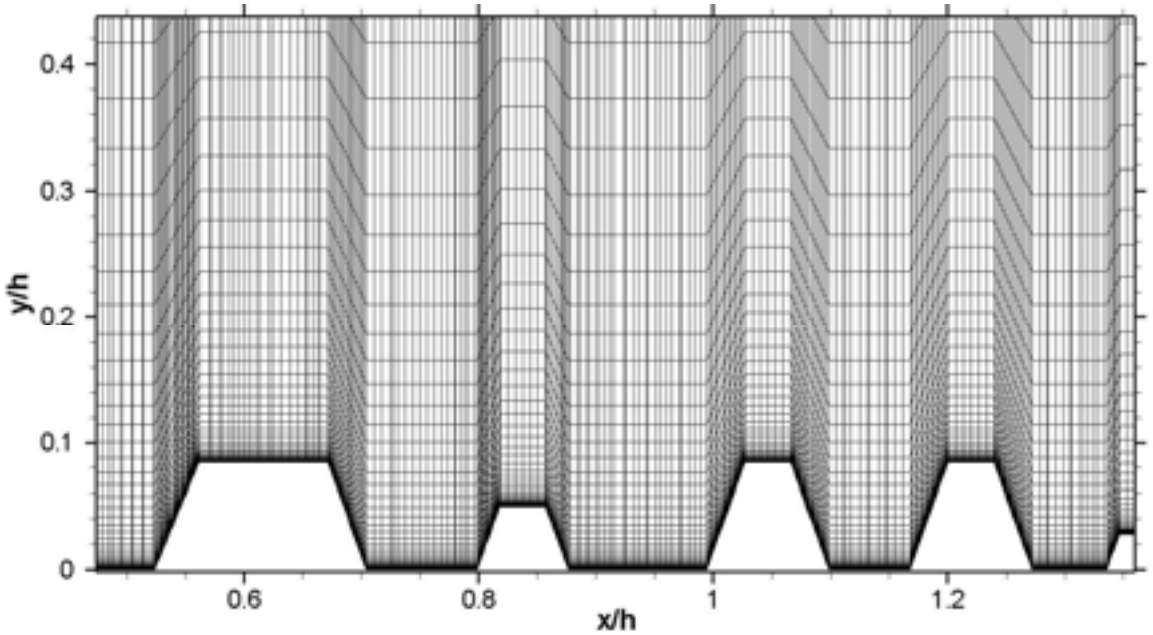

Figure 9: Mesh spacing in the vertical and horizontal along the plane z=0.162h (z=12.5 mm).

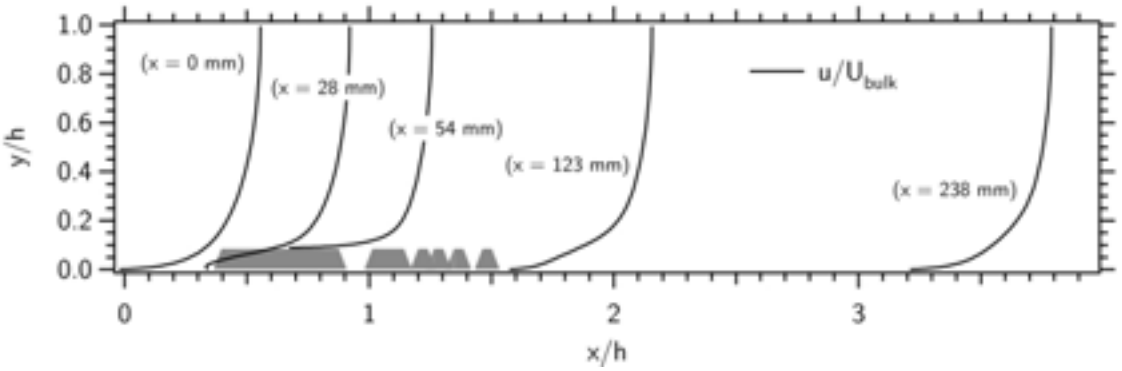

Figure 10: Velocity profiles over cluster as predicted by the SST near-wall solution.

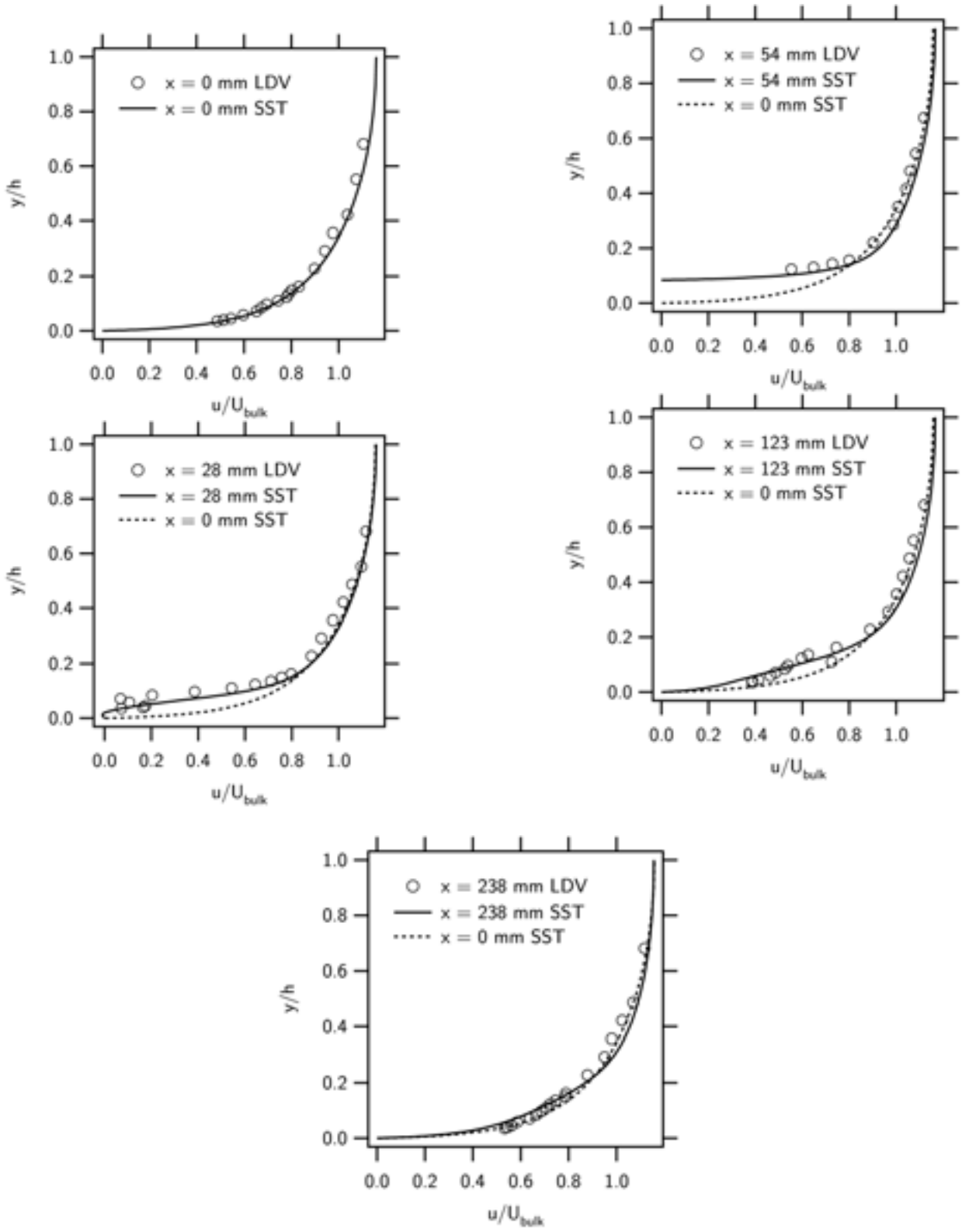

Figure 11: Comparison of experimental and numerical simulation for u at: (a) x=0 mm, (b) x=28 mm, (c) x=54 mm, (d) x=123 mm, and (e) x=238 mm.

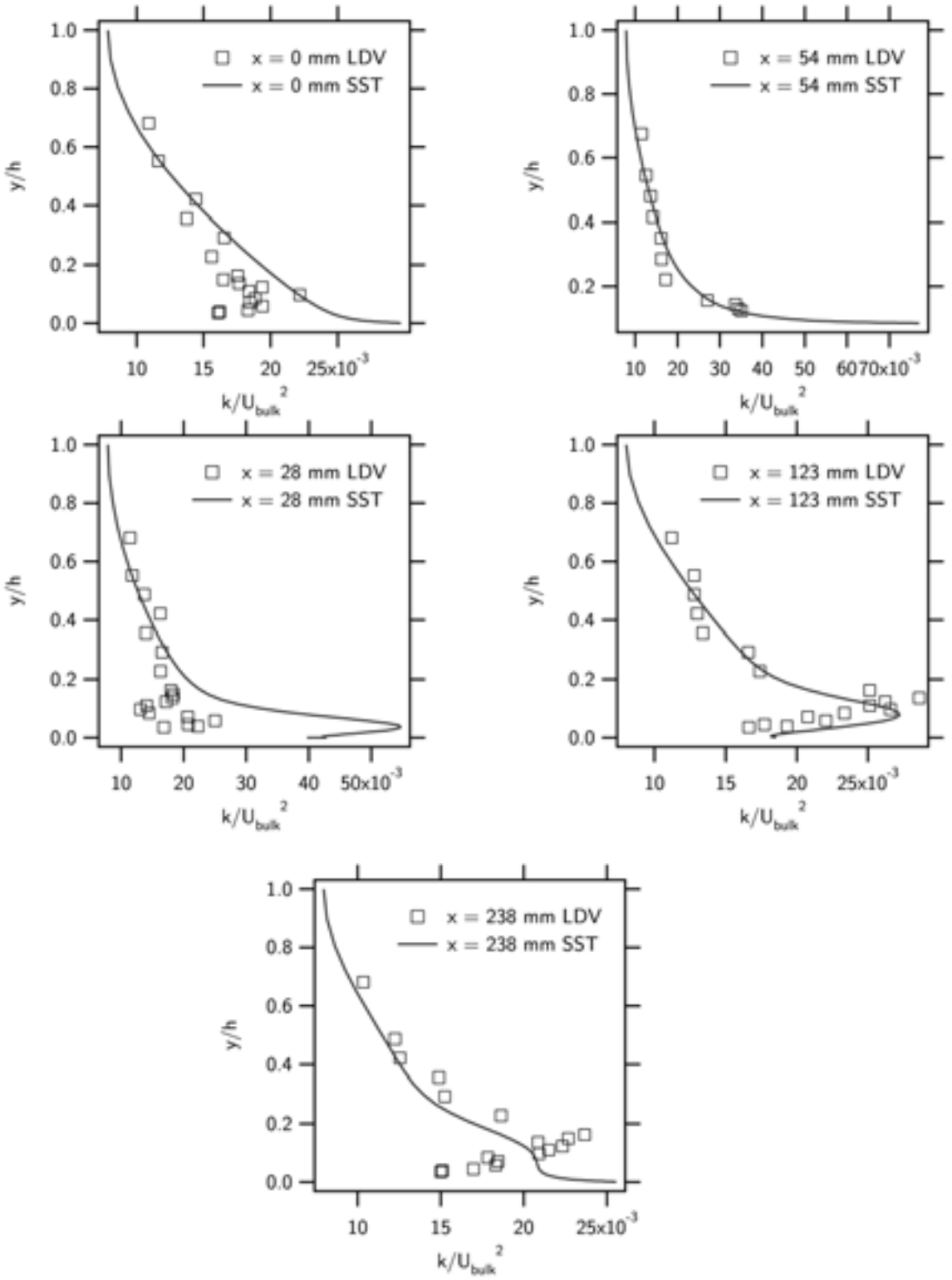

Figure 12: Comparison of experimental and numerical simulation for k at: (a) x=0 mm, (b) x=28 mm, (c) x=54 mm, (d) x=123 mm, and (e) x=238 mm.

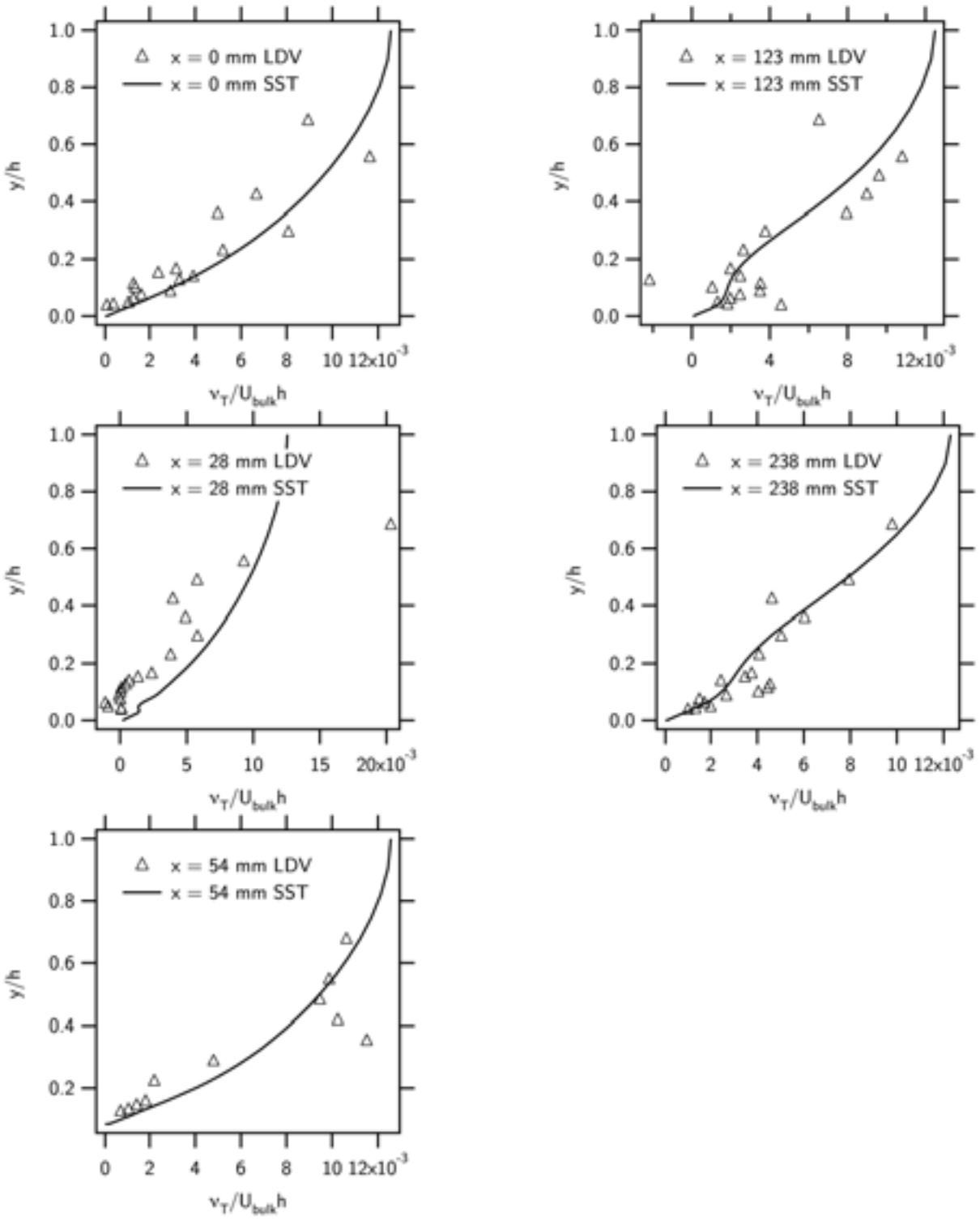

Figure 13: Comparison of experimental and numerical simulation for ν_T at: (a) x=0 mm, (b) x=28 mm, (c) x=54 mm, (d) x=123 mm, and (e) x=238 mm.

III. FIELD COMPONENT

A. Field Study Objectives

The main objectives for the field component of the project were:

1) Characterize the cluster bedform morphologies in natural streams and compare with the morphologies produced in the laboratory for uniform and non-uniform grain sizes.

2) Identify the field geomorphic settings conducive to creating and maintaining cluster bedforms similar to those formed in the laboratory.

3) Characterize the hydraulic parameters, such as velocity, shear stress and near-bed turbulence, necessary to form, maintain and disaggregate sediment clusters.

4) Determine the fate of individual sediment particles within and outside clusters during bed-mobilizing events.

B. Experimental

1. Site Description

The American and Entiat Rivers in central Washington were selected for the field component of the project. Both are unregulated, gravel-bed rivers that drain the eastern slopes of the Cascade Mountains and are part of the Columbia River watershed.

The study site on the American River is a gravel bar and adjacent channel bottom on the left bank of the river immediately downstream of the Pleasant Valley Campground at 46˚ 56’ 45” N. Lat., 121˚ 19’ 10” W. Long. The site is ~15 km upstream of the USGS gaging station on the American River at the junction with the Bumping River (USGS Amer. R. nr Nile, WA). The river at Site 1 is ~15 meters wide, highly sinuous, with a moderate gradient. The valley floor at this site is ~1.75 km wide. About 5 km downstream, the river enters the narrow, steep canyon that characterizes the lower reach of the American River. On the American River the density, spacing, morphology and sediment characteristics of clusters were measured and described in four study plots in different geomorphic settings within the same reach: 1) riffle/bar (inundated by relatively low flows, exposed during lowest flow), 2) high-flow bar (inundated only during high flows, such as annual peaks), 3) edge of low-flow channel thalweg, and 4) center of channel thalweg (plots 3 and 4 continually inundated under low flows). The high-flow gravel bar is on the downstream inside bank of a bend in the channel.

The study area on the Entiat River was located near the middle of the watershed from River km 27-30 (RM 17-19) above the confluence with the Columbia River (Hendrick, 2005). Within this reach we compared two sites in similar geomorphic settings relative to the channel (lateral channel bars), but different settings within the larger scale geomorphology of the river valley. The two study sites on the Entiat River are gravel bars less than 1 km apart along the left-bank channel margin. The sites are immediately upstream and downstream of a constriction formed between the bedrock valley wall and a high, bouldery alluvial fan/terrace. A U.S. Geological Survey gaging station (Entiat R. nr Ardenvoir, no. 12452800), is located in the constriction between the two sites. The major difference in the geomorphic setting of the two sites is the introduction of a coarse sediment component into Site 2, which is derived from erosion of the alluvial fan/terrace. The influence of the coarse sediment is mainly reflected in a significant increase in the size of the anchor clasts forming the sediment clusters (Table 3). The d_{50} of the entrapped sediment within the clusters is the same at both sites (6 cm).

2. Cluster Description

For the purpose of the field study, sediment clusters were defined as an anchor clast(s) that impedes the progress of two or more sediment particles. In addition, due to the irregular microscale topography of the gravel bars examined for this study, clusters were also defined as those protruding at least 3 cm above the normal gravel bed surface of the immediate surrounding area within a 50-cm radius of the cluster. Only those clusters with anchor clasts larger than 5 cm were defined as clusters.

Clusters can form in various sizes and morphologies. The naming scheme for the different cluster geometries varies by study (Brayshaw, 1984; Wittenberg, 2002; Papanicolaou and Schuyler, 2003; Strom et al., 2004a; Strom et al., 2004b), but in general refers to a similar set of cluster forms. The naming scheme used in this field study was as follows:

- Upstream triangle: one or more anchor clasts that trap particles on the stoss, or upstream, side of the anchor, with minimal particles (usually sand sized) in the wake, or downstream, side of the anchor.
- Downstream triangle: one or more anchor clasts that trap particles on the wake side of the anchor, with minimal particles on the stoss side.
- Diamond: one or more anchor clasts that trap particles on both the stoss and wake sides of the anchor clast(s),

- Ring: rounded formation of anchor clasts that trap particles in the center; typically does not have a wake or stoss
- Parallel line: particles (typically of similar size) that form in a line parallel to flow direction.
- Transverse line: particles (typically of similar size) that form in a line perpendicular to flow direction.

C. Field Methods

The field methods included determining the cluster morphology, describing the geomorphic settings and tracking the evolution of cluster form before and after flow events that inundated the site. Accomplishing these tasks involved 1) identifying and marking the clusters, 2) describing and photographing each cluster, 3) surveying cluster locations using a total station laser theodolite, 4) surveying channel cross sections for hydraulic modeling, 5) installing a stage monitoring instrument (American River site), 6) measuring flow velocity at known stages, and 7) describing geomorphic settings of gravel bars containing clusters. After each flow event that was large enough to entrain and transport gravel on the bed, the marked clusters were re-photographed.

At each site, study plots were measured and marked on the gravel bars and the most prominent clusters within each plot were identified and marked to track the evolution of the cluster position and form through inundating flow events. Each identified cluster was numbered, marked with permanent markers and paint, and its position was surveyed with a total station laser theodolite. Two photographs of each cluster were taken, the first using the widest angle setting on the camera from a consistent height so that a similar scale for all the clusters could be documented, and a close-up photograph of the cluster, which yielded a more detailed documentation of the cluster with varying scales for different sized clusters. Each photograph included a 15-cm scale and was taken with the photographer standing above the cluster, facing the stream with flow direction from right to left. For each cluster, the following characteristics were recorded: cluster identification number, cluster form (from naming scheme above) orientation to flow direction, number of anchor clasts, size of the largest anchor within each cluster (long, short, and intermediate axis), overall length and width of cluster, total number and approximate d_{50} of particles greater than 3 cm being impeded by the anchor(s).

In addition to identifying, measuring, and describing baseline clusters for tracking evolutionary patterns, every cluster within each plot that met the pre-defined criteria was numbered and briefly described, but not marked. This analysis was used to better define the spatial distribution, density, and morphologies of clusters at each site.

Multiple channel cross-sections were surveyed throughout the study reaches for hydraulic modeling. The HEC-RAS hydraulic modeling program (U.S. Army Corps of Engineers Hydrologic Engineering Center, 2004) was used to conduct a 1-dimensional, steady flow analysis of the reach to determine the stage/discharge relation for the relevant peak flows at each site. The end points of each cross-section were monumented with stakes. A stage monitoring instrument and data recorder made by Global Water Instruments were installed at the American River to record the peak stage. The instrument automatically recorded the stage every 30 minutes for several months, and was used to calibrate the HEC-RAS modeled peak discharge at the site with the discharge value for the same event at the USGS gaging station downstream. On the Entiat River the USGS gaging station was in close proximity to the study sites, and no calibration was necessary.

D. Shear Stress Calculations

Two equations were use to calculate and compare the critical shear stress required to entrain individual, "isolated" particles sitting atop the gravel bed versus those in sediment clusters: the Shields equation and a modified equation from Komar (1989). These equations were applied at the Entiat River study sites (Hendrick, 2005), which experienced multiple bed-mobilizing events during the course of the study. Shields developed one of the first equations for determining the dimensionless critical shear stress, also referred to as the Shields Parameter ($\boldsymbol{\tau}^*_{cri}$), required to entrain sediment particles of a given size and density (Buffington and Montgomery, 1997). The Shields equation is given by:

$$\boldsymbol{\tau}^*_{cri} = \boldsymbol{\tau}_{cri} / (\rho_s - \rho) g D_i \qquad (18)$$

where $\boldsymbol{\tau}_{cri}$ is the mean shear stress in Newtons per meter squared (N/m^2) at initial motion of the grain size of interest D_i (mm), ρ_s equals the density of sediment (g/cm^3), ρ equals the density of water (g/cm^3), and g equals the acceleration of gravity (m/s^2). The mean shear stress value ($\boldsymbol{\tau}_{cri}$)

was estimated from water-surface elevations, mean flow depths, and the specific weight of water given by the HEC-RAS hydraulic model and the Duboys equation (Chow, 1959). For this study the grain size of interest (D_i) was the mean intermediate axis diameter of the five largest particles that were entrained by a given flow event (either isolated or clustered particles).

The Shields equation was chosen for this study for two reasons. First, it was developed for determining the shear stress required to entrain individual particles atop a layer of uniform sediment. Although the sediment is not uniform in the Entiat River, some of the particles are sitting on top of the bed, and are assumed to be isolated from hiding effects of the larger sized particles. Second, although the use of the bed shear stress to model sediment entrainment is limited because of above-mentioned simplifying assumptions, it is useful as a comparison of clustered versus non-clustered particles that are adjacent to each other on the same gravel bed. It eliminates or reduces some of the complex factors used in other shear stress equations to determine average shear stress across the entire channel bed, such as effects of channel shape on large-scale turbulence, general degrees of sediment packing, sediment-size distribution, sediment shape, pivot angles, degree of sorting, and microscale flow velocities around individual particles (Knighton, 1998; Buffington and Montgomery, 1997).

A second equation given by Komar (1989), which accounts for larger particle size fractions in a non-uniform sediment-size distribution, was also used to compare the critical shear stress values for isolated vs. clustered particles. The Komar equation provides a general and simplistic equation for selective-entrainment of varying particle size fractions in a non-uniform sediment-size distribution, and is given by:

$$\boldsymbol{\tau}^*_{cri} = a(D_i / D_{50})^{b} \qquad (19)$$

where $\boldsymbol{\tau}^*_{cri}$ is the critical shear stress required to entrain particles (dimensionless; similar to the Shields Parameter), *a* and *b* are coefficients (−0.045 and −0.65, respectively). The *a* and *b* coefficients were developed by Komar (1989) based on comparisons of previous selective entrainment data, each of which was developed using field-based methods (Milhous, 1973; Carling, 1983; Hammond et al., 1984). The D_i in Equation (19) represents the mean b-axis diameter of the five largest isolated or clustered particles that were entrained by a given flow event, with respect to the average grain size of the bed (D_{50}).

Using both the Shields and Komar equations allowed for the testing of one of the main hypotheses of this study, which was that entrainment of particles within clusters will require a higher critical shear stress than entrainment of isolated particles, thus reducing sediment transport during high flow events. Of course, the use of any empirical equation in a field-based study comes with assumptions. The main assumptions of the Shields equation include uniform grain size that is spherical in shape, a limited degree of bed packing, and a planar bed surface. These assumptions were considered acceptable given the advantage of using this simplistic, basic shear stress equation to determine the differences in critical shear stress values for individual particles isolated on the bed compared to those in clusters. The Komar equation also has assumptions, one of which is that the standardized coefficients can be applied to the Entiat River, and can account for many of the factors that affect average bed shear stress. Potential errors in the actual critical shears stress values, including under and/or over estimations, are acceptable if they are systematic for both isolated and clustered particles because it was the difference between these values that was of interest for this study.

E. Field Study Results

Previous laboratory flume studies (Strom, 2002; Papanicolaou et al., 2003) produced the following evolutionary cycle of cluster morphologies under increasing flows: no cluster→ two-particle cluster→ comet→ triangle→ rhomboid→ cluster break-up. We therefore hypothesized a similar morphology and evolution for the clusters in the field sites: 1) transverse line clusters are incipient forms that would ultimately transform into upstream or downstream triangles; 2) upstream and downstream triangle clusters are intermediate cluster forms which ultimately form diamond clusters; and 3) diamond clusters are the final cluster form and are therefore the most stable. This hypothesis was mainly tested on the Entiat River, as the American River did not a experienced bed-mobilizing discharge during the 2-year period of the field study.

Six general categories of cluster morphologies were observed at the study sites on the American and Entiat Rivers. The six types include upstream triangle, downstream triangle, diamond, ring, line and transverse line (Fig. 14). These cluster morphologies are virtually identical to those formed in laboratory flume studies (Strom, 2002; Papanicolaou et al. ,2003) using glass spheres. The similarity between the clusters in the laboratory and natural settings

validates the cluster morphology results obtained in the flume and supports the applicability of the results from the flume experiments to sediment transport in natural streams.

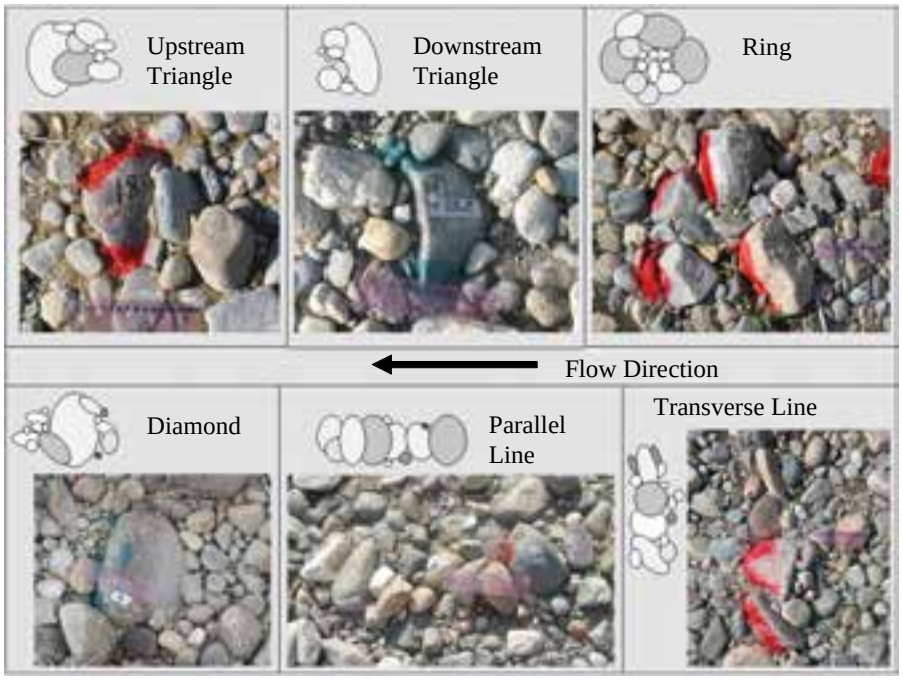

Figure 14. Typical cluster geometries found along Entiat River. Channel position is at the top of the sketch or photograph with flow direction from right to left (Hendrick, 2005).

Table 3. Cluster and Surface-Sediment Characteristics, American and Entiat River Sites

American River, Site 1

Plot #	Geomorphic Setting	Dominent Cluster Morphology	Mean Cluster Size (cm) Length	Mean Cluster Size (cm) Width	Mean Anchor Size (axes) Long	Mean Anchor Size (axes) Interm.	Mean Anchor Size (axes) Short	d50 Surface Sediment
1	Riffle/Bar	upstr. tri. / parallel line	33.9	26.4	16.2	9.9	6.2	6.7
2	High-flow bar	upstream triangle	36.4	25.7	19.2	13.6	7.3	5.9
3	Thalweg edge	upstr. tri. / ring	35.1	31.7	14.7	9.5	6.2	6.2
4	Thalweg center	upstream triangle	29.8	25.4	14.1	10.2	6.2	6.2

Entiat River; Site 1 (upstream of constriction)

Plot #	Geomorphic Setting	Dominent Cluster Morphology	Mean Cluster Size (cm) Length	Mean Cluster Size (cm) Width	Mean Anchor Size (axes) Long	Mean Anchor Size (axes) Interm.	Mean Anchor Size (axes) Short	d50 Surface Sediment
1	Bar	upstream triangle	23.5	18.6	13.9	8.7	5.7	3.6
2	Bar	upstream triangle	21.6	15.6	12.6	8.2	4.5	3.5
3	Bar	no dominent shape	25.5	19.5	14.0	8.3	5.3	3.6

Entiat River; Site 2 (downstream of constriction)

Plot #	Geomorphic Setting	Dominent Cluster Morphology	Mean Cluster Size (cm) Length	Mean Cluster Size (cm) Width	Mean Anchor Size (axes) Long	Mean Anchor Size (axes) Interm.	Mean Anchor Size (axes) Short	d50 Surface Sediment
1	Bar	upstream triangle	33.6	26.4	20.8	14.7	7.2	5.9

1. American River Study Site.

The distribution of cluster morphologies in different geomorphic settings on the American River is summarized in Table 4. The thalweg plots represent the low-flow channel that is inundated with water even at low flows (late summer). The riffle/bar is at the edge of the low-flow channel and is inundated through mid summer. The high-flow bar is inundated only during high flows, (less than 1 month in May-June, 2003).

Table 4. Cluster Morphology at American River Site.

Plot #	Area (m^2)	Geomorphology	Proportion of Clusters in Each Morphology Category: Upstream Triangle	Downstrm Trianglel	Diamond	Parallel Line	Trans Line	Ring/Rectan	Mean # Anchors	Total # Clusters	Density (cluster/m^2)
1	25	Riffle/Bar	0.31	0.08	0.12	0.16	0.10	0.20	2.32	53	2.12
2	25	High-flow Bar*	0.29	0.04	0.09	0.41	0.00	0.16	1.45	77	3.08
3	4	Thalweg edge	0.36	0.05	0.00	0.09	0.14	0.36	2.64	22	5.5
4	4	Thalweg center	0.55	0.00	0.00	0.05	0.10	0.25	2.45	20	5

*Described clusters across entire bar, not all in plot

The upstream triangle cluster form was the most common in the thalweg and riffle plots and was the second most common form in the high-flow bar. This form consists of one or more

anchor clasts with the long axis transverse to the flow and an accumulation of smaller clasts upstream. The parallel line of imbricated particles was most common on the high-flow bar and progressively decreased in abundance in the plots closer to the thalweg. The ring/rectangle form was much more abundant in the low-flow thalweg and riffle/bar plots than the high-flow bar. This form consists of multiple clasts that form either a ring or rectangle shape and collectively serve as an anchor against which smaller clasts accumulate.

The density of clusters was greatest in the thalweg plots, although the clusters themselves were not as well defined as in the high-flow bar. Many clusters in the thalweg and riffle/bar plots consisted of multiple anchors or ring forms that collectively trapped additional gravel clasts, and were often linked together with shared particles in adjacent clusters in a reticulated pattern. In contrast, the clusters in the high-flow bar were mainly single anchor clasts that were completely separate from adjacent clusters.

Our interpretation of the variations in cluster morphology and density among the different parts of the channel at the American River site is that the clusters in the thalweg and low riffle/bar plots are subjected to flows of longer duration and greater velocity. This situation either leads to formation of different cluster morphologies initially, or rearrangement and partial disintegration of initial clusters after the original deposition to form more linked clusters with multiple anchor clasts. The clusters on the high-flow bar are less likely to be altered from their original form, as they are only inundated for brief periods, and only a subset of the annual peak flows are large enough to mobilize them.

On the American River the 2003 peak flow was 31.5 m^3/sec and the 2004 peak flow was 24 m^3/sec, which are moderate-sized annual peaks compared to the historic record. No flows during the 2-year period were sufficient to mobilize the sediment clusters, and all cluster forms were therefore stable throughout the study period. However, individual sediment particles were added, moved and removed from the clusters. The diamond clusters experienced the greatest amount of individual sediment movement through the stable cluster bedforms and the transverse lines the least.

2. Entiat River Study Site

The results from the Entiat River are summarized in detail in the Master's thesis by Ross Hendrick (2005). On the Entiat River, the evolution of cluster bedforms and movement

of individual sediment particles within clusters were monitored for 4 peak flows that inundated the study site. The peak flows were Oct., 2003, 57 m^3s^{-1}; Nov. 2003, 13 m^3s^{-1}; May 2004, 39 m^3s^{-1}, and Jan. 2005, 22 m^3s^{-1} (Fig. 15). Sediment cluster bedforms had a measurable impact on sediment entrainment during the two intermediate flow events of 22 and 39 m^3s^{-1} that inundated the gravel bar at the study site. Under these flows, the critical shear stress required to entrain sediment particles was 38-51% greater for sediment within clusters than for isolated sediment particles on the gravel bar. All clusters were mobilized during the highest peak in the 2-year record, 57 m^3s^{-1}, which occurred in October, 2003. Therefore the clusters did not significantly impact the overall sediment transport during this event, as the entire bed was mobilized at the study site. No measurable sediment movement occurred within the clusters during the lowest inundation event of 13 m^3s^{-1}. The mean annual peak flow on the Entiat River is ~80 m^3s^{-1}, which means that on average, sediment clusters on this river are likely at least partially mobilized and reformed on a semi-annual basis. At site 1 on the Entiat River, which had a fairly well-sorted sediment size distribution, the diamond cluster form was the most stable over the 2-year period. At site 2, with a greater range of sediment sizes and larger anchor clasts, all cluster forms were equally stable.

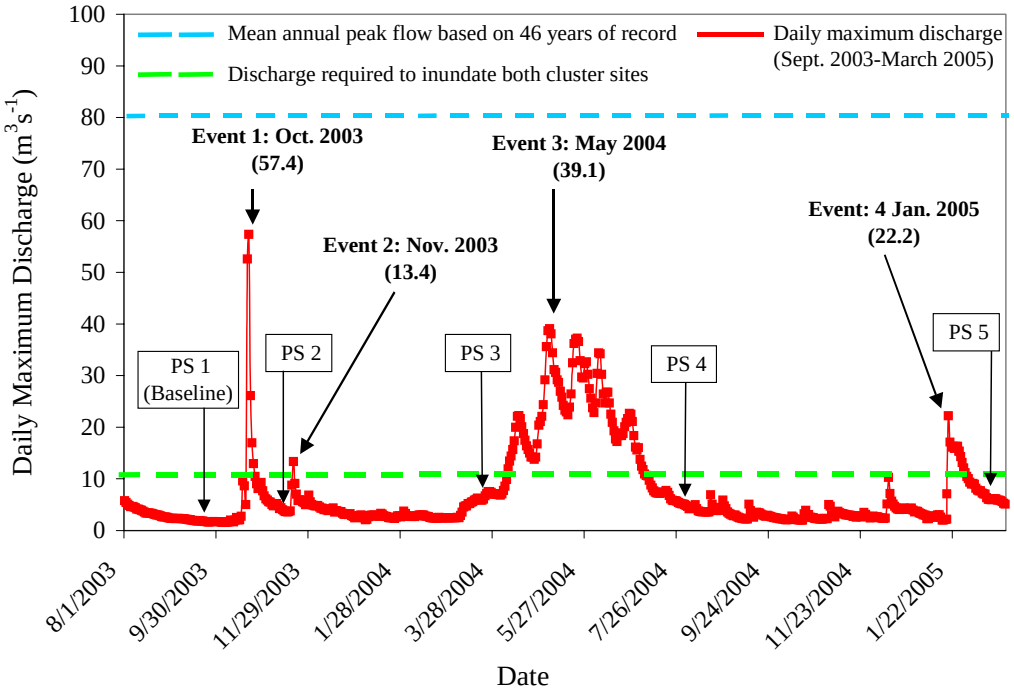

Figure 15. Daily maximum discharge values on the Entiat River during period of study. PS = photograph set of clusters was taken. Discharge data obtained from U.S. Geological Survey (2005) streamflow gage located at Rkm 29 (RM 18), between sites 1 and 2 (Hendrick, 2005).

On the Entiat River, 37 clusters were marked and rephotographed after each inundation event; 17 of these evolved from one cluster morphology to another during the 4 high flow events observed during this study (Fig. 16). The number of original clusters marked for tracking decreased with each flow event, as clusters were destroyed. However, the total number of clusters on the bar did not decrease. Both general observation of the gravel bar after each flow event and detailed examination of the plots after event 3 showed that many new clusters formed after each event. However, only the original tagged clusters and their evolution and/or destruction after each flow event are discussed, and no newly formed clusters were added to the original dataset used for tracking cluster evolution.

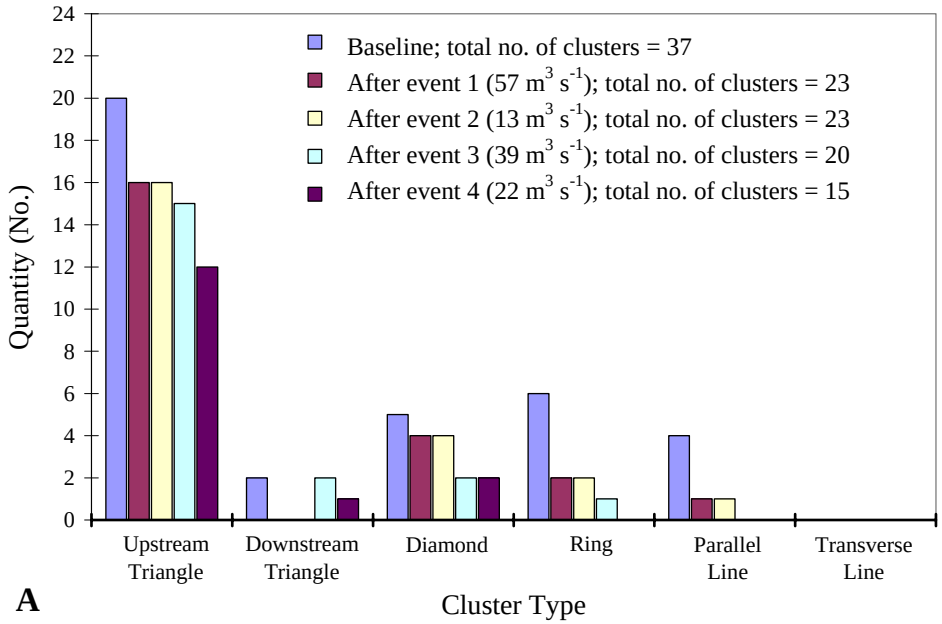

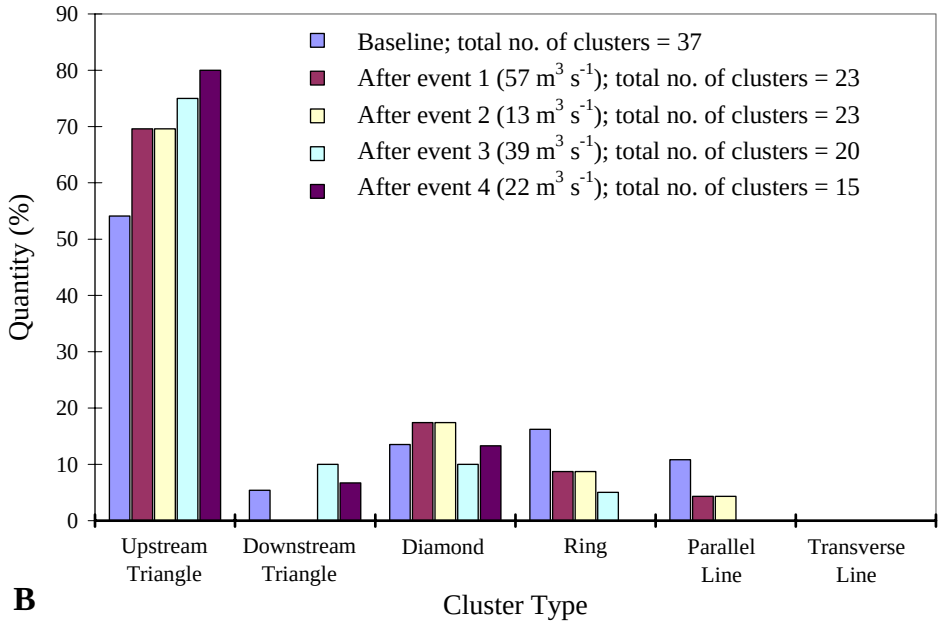

Figure 16. Cluster evolution for Entiat River Site 1 (all plots). (A) Number of each cluster morphology that were marked for the baseline dataset and relocated after each observed flow event during period of study. (B) Percentage of each cluster type out of the total number of clusters for the baseline dataset and after each observed flow event during period of study (Hendrick, 2005).

No consistent evolutionary pattern was observed in the cluster morphology on the Entiat River, and only one upstream triangle evolved into a diamond cluster type. This lack of an apparent evolutionary cycle may be due to the order of the flow events observed during this study, with the largest event first, followed by the smallest event, a mid-sized event, and then another small event. These flow patterns are different from the experimentally generated smallest-to-largest flow conditions produced by Strom (2002) and Papanicolaou et al. (2003), which produced the following evolutionary cycle of cluster morphologies under increasing flows: no cluster→ two-particle cluster→ comet→ triangle→ rhomboid→ cluster break-up. Many of the marked clusters were destroyed at site 1 during flow events 1, 2, and 3, which may have "reset" the cluster cycle after each flow event. If the upstream triangle represents the initial cluster morphology after two-particle and comet clusters, which were not considered in the field study, this resetting of the cluster cycle may explain why the upstream triangle is the most abundant cluster morphology in the Entiat River.

Brayshaw (1985) and Reid et al. (1992) suggested that mobilization of anchor clasts must occur prior to cluster destruction, while de Jong (1991) and Billi (1988) suggested clustered particles could be removed without anchor clast mobilization. Results from the Entiat River indicate that at site 1, with nearly uniform sediment-size distribution, both methods of cluster destruction occurred. However, results from site 2, with a bi-modal sediment-size distribution, suggest that anchor clast mobilization must occur prior to cluster destruction, supporting the results of Brayshaw (1985) and Reid et al. (1992). Therefore, while both these interpretations of cluster destruction appear to be correct, results from the present study indicate that sediment-size distribution is a major controlling factor in the method of cluster destruction.

Comparisons of the dimensions of the largest isolated particles vs. cluster particles that were moved during flow events on the Entiat Rivers indicate that the sediment clusters inhibit entrainment of gravel particles. The maximum size of particles entrained from sediment clusters was consistently less than that of adjacent isolated particles during the same flow events (Fig. 17). This difference was not due to a lack of larger particles available in the sediment clusters. Critical shear stress values calculated from the Shields equation ranged from 0.014 to 0.144 for isolated particles and 0.022-0.142 for clustered particles within all plots at sites 1 and 2. The critical shear stress values calculated from the Komar equation were, in general, smaller, ranging from 0.026 to 0.034 for isolated particles and 0.028-0.047 for clustered particles within all plots

at sites 1 and 2 (Fig. 18). The increases in the critical shear stresses required to entrain clustered particles were consistent with previous field and laboratory flume experiments (Reid et al., 1992; Montgomery et al., 1996; Buffington and Montgomery, 1997; Church et al., 1998; Papanicolaou et al., 2003; Strom et al., 2004b).

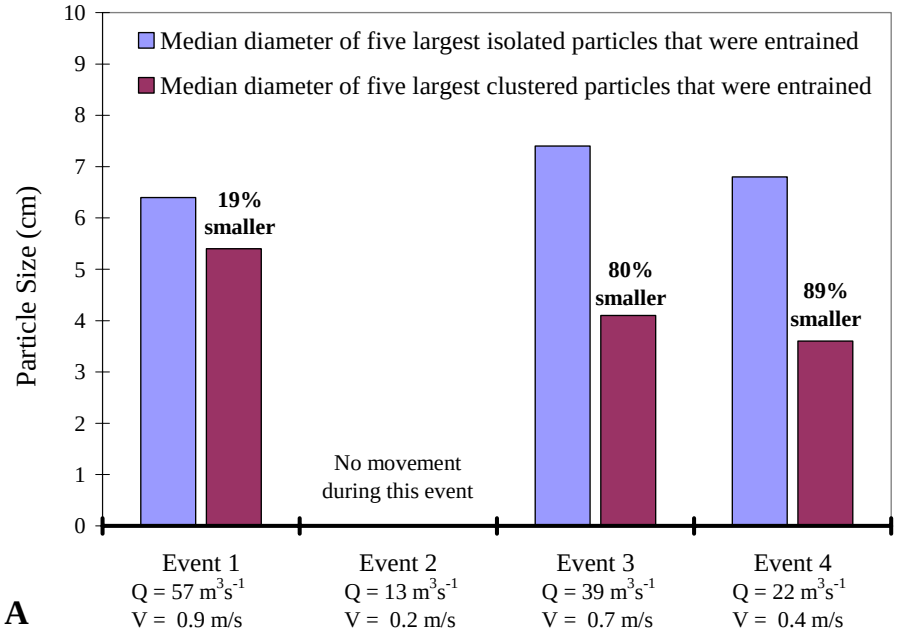

Figure 17. Median diameter of largest isolated and clustered particles entrained by each flow event at Entiat River Site 1, Plot 1. Percentage smaller represents the percentage difference between the size of isolated and clustered particles. Differences were statistically significant with a *P* value of 0.0034. Results from other plots at Site 1 showed a similar pattern (Hendrick, 2005).

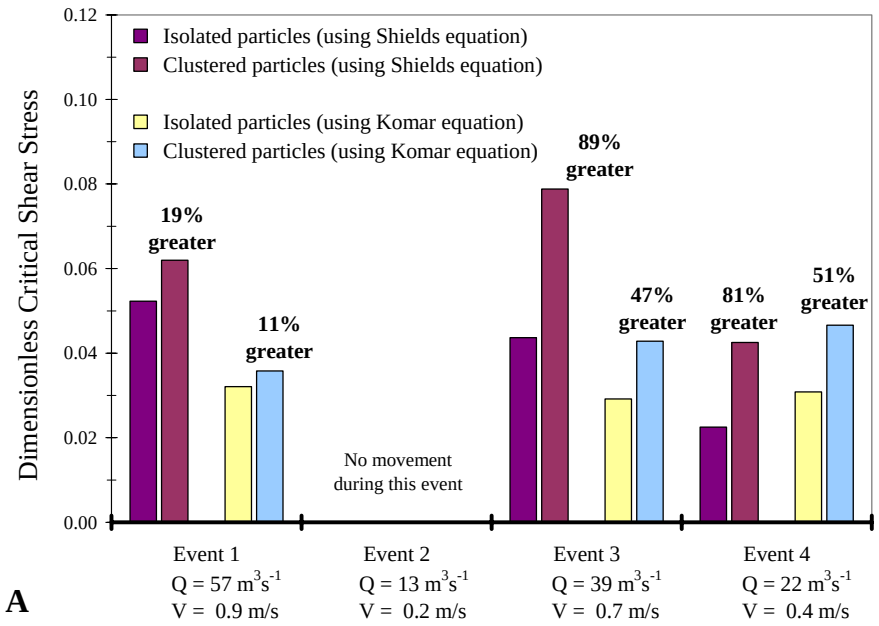

Figure 18. Critical shear stress values for largest isolated and clustered particles entrained by each flow event at Entiat River Site 1, Plot 1. Percentage greater represents the percentage difference between the critical shear stress required to entrain the isolated and clustered particles. Differences were statistically significant with *P* values of 0.0299 using the Shields equation and 0.0125 using the Komar equation. Other plots at Site 1 showed similar patterns (Hendrick, 2005).

The values calculated by the Komar equation were well within the range of previous studies, suggesting accurate estimations of critical shear stress values based on field data from the present study (Hendrick, 2005). Some values calculated by the Shields equation were higher than 0.087 (plot 3 at site 1 for events 1, 3, and 4), suggesting that the Shields equation may be over-predicting critical shear stress values, which may be expected given the simplistic nature of this equation (Strom, 2002; Papanicolaou et al., 2003). Values derived from the Shields equation therefore provide upper-end estimates of the shear stress required to entrain both clustered and isolated particles within the study reach. These values would prove useful in determining the range of flows required to entrain similar-sized sediment within similar river systems, especially if those rivers have regulated flow regimes so that river managers can design maintenance flows that are large enough to transport regular sediment fluxes but do not create significant erosion.

REFERENCES

Biggs, B. J. F., Duncan, M. J., Francoeur, S. N., and Meyer, W. D., 1997, Physical characterisation of microform bed cluster refugia in 12 headwater streams, New Zealand: New Zealand Journal of Marine and Freshwater Research, v. 31, no. 4, p. 413-422.

Billi, P., 1988, A note on cluster bedform behaviour in a gravel-bed river: Catena, v. 15, no. 5, p. 473-481.

Boelman, S. F., and Stein, O. R., 1997, Performance of instream boulder clusters in a cobble-bed river, *in* Environmental and coastal hydraulics: Protecting the aquatic habitat: San Francisco, CA, p. 1049-1054.

Brayshaw, A. C., 1984, Characteristics and origin of cluster bedforms in coarse-grained alluvial channels, *in* Koster, E. H., and Steel, R. J., eds., Sedimentology of gravels and conglomerates: Calgary, Canadian Society of Petroleum Geologists, p. 77-85.

Brayshaw, A. C., 1985, Bed microtopography and entrainment thresholds in gravel-bed rivers: Geological Society of America Bulletin, v. 96, no. 2, p. 218-223.

Brayshaw, A. C. (1984). “Characteristics and origin of cluster bedforms in coarse-grained alluvial channels,” Sedimentology of Gravels and Conglomerates, E. H. Koster and R. J. Steel, eds., Canadian Society of Petroleum Geologist, 10, 77–85.

Buffin-Bélanger, T., and Roy, A. G. (1998). “Effects of a pebble cluster on the turbulent structure of a depth-limited flow in a gravel-bed river,” Geomorphology, 25, 249–267.

Buffington, J. M., and Montgomery, D. R., 1997, A systematic analysis of eight decades of incipient motion studies, with special reference to gravel-bedded rivers: Water Resources Research, v. 33, no. 8, p. 1993-2029.

Carling, P. A., 1983, Threshold of coarse sediment transport in broad and narrow natural streams: Earth Surface Processes and Landforms, v. 8, no. 1, p. 1-18.

Cebeci, T., and Bradshaw, P. (1977). Momentum Transfer in Boundary Layers, Hemisphere Publishing Corporation.

Chow, V. T., 1959, Open-channel hydraulics: New York, McGraw-Hill, Inc., 680 p.

Church, M., Hassan, M. A., and Wolcott, J. F., 1998, Stabilizing self-organized structures in gravel-bed stream channels: Field and experimental observations: Water Resources Research, v. 34, no. 11, p. 3169-3179.

Clifford, N. J., Robert, A., and Richards, K. S. (1992). “Estimation of flow resistance in gravel-bedded rivers: a physical explanation of the multiplier of roughness length,” Earth Surface Processes and Landforms, 17, 111–126.

Dal Cin, R. (1968). ‘‘‘Pebble clusters”: Their origin and utilization in the study of palaeocurrents,” Sedimentary Geology, 2, 233–241.

Dal Cin, R., 1968, Pebble clusters: Their origin and utilization in the study of palaeocurrents: Sedimentary Geology, v. 2, p. 223-324.

De Jong, C., 1991, A reappraisal of the significance of obstacle clasts in cluster bedform dispersal: Earth Surface Processes & Landforms, v. 16, no. 8, p. 737-744.

de Jong, C. (1995). “Temporal and spatial interactions between river bed roughness, geometry, bedload transport and flow hydraulics in mountain streams - examples from Squaw Creek, Montana (USA) and Schmiedlaine/Lainbach (Upper Germany),” Berliner Geographische Abhandlungen, 59, 229.

FLUENT Inc. (2003). FLUENT 6.1 users guide, Lebanon, New Hampshire.

Hammond, F. D., Heathershaw, A. D., and Langhorne, D. N., 1984, A comparison between Shields’ threshold criterion and the movement of loosely packed gravel in a tidal channel: Sedimentology, v. 31, p. 51-62.

Hassan, M. A., and Church, M., 2000, Experiments on surface structure and partial sediment transport on a gravel bed: Water Resources Research, v. 36, no. 7, p. 1885-1895.

Hassan, M. A., and Reid, I. (1990). “The influence of microform bed roughness elements on flow and sediment transport in gravel bed rivers,” Earth Surface Processes and Landforms, 15, 739–750.

Hendrick, R.R., 2005, The Role of Geomorphic Features and Hydrologic Processes on Sediment Clusters in Gravel-Bed Rivers, Washington: A Field-Based Approach, M.S. Thesis, Central Washington University, 117 p.

Hodskinson, A., and Ferguson, R. I. (1998). “Numerical modelling of separated flow in river bends: Model testing and experimental investigation of geometric controls on the extent of flow separation at the concave bank,” Hydrological Processes, 12, 1323–1338.

Karim, O. A., and Ali, K. H. M. (2000). “Prediction of flow patterns in local scour holes caused by turbulent water jets,” Journal of Hydraulic Research, 38(4), 279–288.

Kirkil, G., Constantinescu, G., and Ettema, R. (2005). “The horseshoe vortex system around a circular bridge pier on equilibrium scoured bed,” ASCE/EWRI World Water & Environmental Resources Congress, Anchorage, AK, volume 173, 414.

Kironoto, B. A., and Graf, W. H. (1994). “Turbulence characteristics in rough uniform open-channel flow,” Proc. Instn Civ. Engrs Wat., Marit. & Energy, 106, 333–344.

Knighton, D., 1998, Fluvial forms and processes: A new perspective: New York, Oxford University Press, Inc., 383 p.

Komar, P. D., 1989, Flow-competence evaluations of the hydraulic parameters of floods: An assessment of the technique, *in* Baven, K., and Carling, P., eds., Floods: Hydrological, sedimentological and geomorphological implications: Hoboken, New Jersey, John Wiley & Sons Ltd, p. 265.

Kozlowski, B., and Ergenzinger, P. (1999). “Ring structures - a specific new cluster type in steep mountain torrents,” XXVII IAHR Congress Proceedings Graz, 410.

Krogstad, P. A., and Antonia, R. A. (1999). “Surface roughness effects in turbulent boundary layers,” Experiments in Fluids, 27, 450–460.

Lane, S. N., Hardy, R. J., Elliot, L., and Ingham, D. B. (2004). “Numerical modeling of flow processes over gravelly surfaces using structured grids and numerical porosity treatment,” Water Resources Research, 40(1), W01302.

Lane, S., Bradbrook, K., Richards, K., Biron, P., and Roy, A. (1999). “The application of computational fluid dynamics to natural river channels: three-dimensional versus two-dimensional approaches,” Geomorphology, 29, 1–20.

Lien, F. S., and Yee, E. (2004). “Numerical modelling of the turbulent flow developing within and over a 3-d building array, part I: A high-resolution Reynolds-Averaged Navier-Stokes approach,” Boundary-Layer Meteorology, 112, 427–466.

McLaughlin, D. K., and Tiederman, W. G. (1973). “Biasing correction for individual realization of laser anemometer measurements in turbulent flows,” The Physics of Fluids, 16(12), 2082–2088.

Menter, F. R. (1994). “Two-equation eddy-viscosity turbulence models for engineering applications,” AIAA Journal, 32(8), 1598–1605.

Milhous, R. T., 1973, Sediment transport in a gravel-bottomed stream [Unpublished Ph.D. thesis]: Corvallis, Oregon State University, 232 p.

Millar, R. G. (1999). “Grain and form resistance in gravel-bed rivers,” Journal of Hydraulic Research, 37(3), 303–312.

Montgomery, D. R., Quinn, T. P., Buffington, J. M., Peterson, N. P., and Schuett-Hames, D., 1996, Stream-bed scour, egg burial depths, and the influence of salmonid spawning on bed surface mobility and embryo survival: Canadian Journal of Fisheries and Aquatic Sciences, v. 53, no. 5, p. 1061-1070.

Morris, H. M. (1955). “Flow in rough conditions,” Transactions ASCE, 120, 373–398.

Naden, P. S., and Brayshaw, A. C., 1987, Small- and medium-scale bedforms in gravel-bed rivers, *in* Richards, K., ed., River channels: IBG special publication, 18: Leeds, United Kingdom, Basil Blackwell, p. 249-271.

Nezu, I., and Nakagawa, H. (1993). Turbulence in open-channel flows, A. A. Balkema, Rotterdam.

Nicholas, A. P. (2001). “Computational fluid dynamics modelling of boundary roughness in gravel-bed rivers: an investigation of the effects of random variability in bed elevation,” Earth Surface Processes and Landforms, 26, 345–362.

Nicholas, A. P., and Sambrook Smith, G. H. (1999). “Numerical simulation of three-dimensional flow hydraulics in a braided channel,” Hydrological Processes, 130, 913–929.

Paola, C., Gust, G., and Southard, J. B. (1986). “Skin friction behind isolated hemispheres and the formation of obstacle marks,” Sedimentology, 33, 279–293.

Papanicolaou, A. N., and Schuyler, A., 2003, Cluster evolution and flow-frictional characteristics under different sediment availabilities and specific gravity: Journal of Engineering Mechanics, v. 129, no. 10, p. 1206-1219.

Papanicolaou, A. N., Strom, K., Schuyler, A., and Talebbeydokhti, N., 2003, The role of sediment specific gravity and availability on cluster evolution: Earth Surface Processes and Landforms, v. 28, no. 1, p. 69-86.

Papanicolaou, A. N., Diplas, P., Dancey, C. L., and Balakrishnan, M. (2001). “Surface roughness effects in near-bed turbulence: Implications to sediment entrainment,” Journal of Engineering Mechanics, 127(3), 211–218.

Papanicolaou, A. N., Diplas, P., Evaggelopoulos, N., and Fotopoulos, S. (2002). “Stochastic incipient motion criterion for spheres under various bed packing conditions,” Journal of Hydraulic Engineering, 128(4), 1–11.

Patel, V. C. (1998). “Perspective: Flow at high Reynolds number and over rough surfaces – Achilles heel of CFD,” Journal of Fluids Engineering, 120, 434–444.

Patel, V. C., Chon, J. T., and Yoon, J. Y. (1991). “Turbulent flow in a channel with a wavy wall,” Journal of Fluids Engineering, 113, 579–586.

Raupach, M. R., Antonia, R. A., and Rajagopalan, S. (1991). “Rough-wall turbulent boundary layers,” Applied Mechanics Review, 44(1), 1–25.

Reid, I., Frostick, L. E., and Brayshaw, A. C., 1992, Microform roughness elements and the selective entrainment and entrapment of particles in gravel-bed rivers, *in* Billi, P., Hey, C. R., and Tacconi, P., eds., Dynamics of gravel-bed rivers: Hoboken, New Jersey, John Wiley & Sons Ltd, p. 253-275.

Shamloo, H., Rajaratnam, N., and Katopodis, C. (2001). “Hydraulics of simple habitat structures,” Journal of Hydraulic Research, 39(4), 351–366.

Sofialidis, D., and Prinos, P. (1999). “Turbulent flow in open channels with smooth and rough flood plains,” Journal of Hydraulic Research, 37(5), 615–640.

Song, T., and Chiew, Y. M. (2001). “Turbulence measurements in nonuniform open-channel flow using acoustic Doppler velocimeter (ADV),” Journal of Engineering Mechanics, 127(3), 219–232.

Strom, K. B., Papanicolaou, A. N., and Constantinescu, G. (2005b). “Rough wall flow using k-turbulence model in FLUENT,” ASCE/EWRI World Water & Environmental Resources Congress, Anchorage, AK, volume 173, 438.

Strom, K. B., Papanicolaou, A. N., Billing, B., Ely, L. L., and Hendrick, R. R. (2005a). “Characterization of particle cluster bedforms in mountain streams,” ASCE/EWRI World Water & Environmental Resources Congress, Anchorage, AK, volume 173, 399.

Strom, K., 2002, Microforms in gravel bed rivers [M.S. thesis]: Pullman, Washington State University, 94 p.

Strom, K., Papanicolaou, A. N., Evangelopoulos, N., and Odeh, M., 2004b, Microforms in gravel bed rivers: Formation, disintegration, and effects on bedload transport: Journal of Hydraulic Engineering, v. 130, no. 6, p. 554-567.

Vanoni, V. A., and Brooks, N. H. (1957). “Laboratory studies of the roughness and suspended load of alluvial streams,” Sedimentation Laboratory Report E68, California Institute of Technology, Pasadena, CA.

Wilcox, D. C. (1993). Turbulence Modeling for CFD, DCW Industries Inc., La Cacada, CA.

Zhou, D., and Mendoza, C. (1993). “Flow through porous bed of turbulent stream,” Journal of Hydraulic Engineering, 119(20), 365–383